Strål
säkerhets
myndigheten
Swedish Radiation Safety Authority

Research

Effect of gamma-irradiation on the redox states of the structural iron in bentonite clay

2023:14

Author: Michael Holmboe, Umeå University, Sweden
Date: November 2023
Report number: 2023:14
ISSN: 2000-0456
Available at www.ssm.se

Strål
säkerhets
myndigheten
Swedish Radiation Safety Authority

Author: Michael Holmboe
Umeå University, Sweden

2023:14

Effect of gamma-irradiation on the redox states of the structural iron in bentonite clay

Date: November 2023
Report number: 2023:14
ISSN: 2000-0456
Available at www.stralsakerhetsmyndigheten.se

SSM perspective

Background
Bentonite clay is used as buffer and backfill material which form engineered barrier in the spent fuel repository. The buffer material surrounding the copper canister will be exposed to gamma and neutron radiations, especially during the first few hundred years after closure of the repository. The redox states of the structural iron in montmorillonite, the dominant mineral in bentonite, have been shown to be sensitive to such irradiation in experimental studies using suspended bentonite. The change of the redox states of the structural iron will result in change of the charge density in montmorillonite mineral structure, which in turn can possibly influence some of the physicochemical properties of bentonite clay, such as swelling. In this study, the focus is on such radiation effect on compacted bentonite.

Results
Molecular dynamics simulations show that the water radiolysis products H2O2, HO• and HOO• are neither strongly interacting nor strongly excluded from the interlayer regions of montmorillonite, although the latter two radicals show some preference to surface regions avoid of isomorphic substitution sites and high density of counter-cations. The same species also show significant affinity to the neutral clay edges modelled.

The changes in the structural Fe(II)/Fe(III) levels due to exposure to gamma radiation for compacted and water-saturated bentonite in general agree with the results in previous experiments obtained using clay dispersions. It generally shows that Fe(II) levels increase in place of Fe(III) with increasing gamma dose.

Investigations by means of isotope-ratio mass spectroscopy (IRMS) using isotopically labelled and non-labelled water show evidence of significant gas formation induced by gamma radiation. The effect of high levels of oxygen present potentially pre-irradiation in some samples should further be investigated before drawing conclusions regarding the gas formation of O2 and CO2.

Relevance
In review of SKB's reporting of safety after closure of the spent fuel repository in the framework of license application, SSM pointed out that the effect of gamma radiation on the redox states of structural iron of montmorillonite in bentonite clay remained to be an issue that needed further investigation. SSM considered that this is a mechanism that can possibly affect the swelling and other properties of the bentonite clay by changing the charge density in the mineral structure of montmorillonite.

Need for further research
The results of this study confirm previous reports that gamma irradiation under anoxic conditions reduces Fe(III) to Fe(II) in montmorillonite mineral and increases radiochemical yields of hydrogen. However, this study also revealed practical difficulties with the methodology used and highlighted limitations in investigating the radiation chemistry of heterogeneous and complex geochemical systems. To overcome some of these hurdles, new synchrotron-based experiments need to be undertaken. Such experiments would not only allow for on-the-fly irradiation and characterisation due to the high flux rates and brilliance at modern synchrotron facilities but also resolve the existing discrepancy in measured Fe(II)/Fe(III) levels between traditional wet chemistry methods (as used in the current study) and previous synchrotron studies that did not take radiation chemical effects into consideration

Project information
Project manager: Jinsong Liu
Project reference: SSM2020-962/4530016

Content

1. Introduction

In the Swedish KBS-3 repository for spent nuclear fuel, the compacted bentonite clay barrier will unavoidably be exposed to ionizing radiation from gamma and neutron radiation (R-99-74 1999; TR-06-09 2006; Holmboe 2011). For bentonite and its main swelling clay mineral montmorillonite, mineral transformation or changes in the overall physicochemical properties is of concern in the overall safety assessment for spent nuclear fuel repository. Because of this the Swedish Radiation Safety Authority (SSM) has identified a need for updating and improving the theoretical understanding of radiation-induced effects on montmorillonite (SSM 2018) in the context of the Swedish KBS-3 concept for final disposal of spent nuclear fuel. Therefore, this study aimed at elucidating the effects of radiation-induced redox changes on compacted bentonite clay under repository-like conditions, scrutinizing prior research performed on dilute clay dispersions.

1.1. Clay buffer exposure to ionizing radiation

From the radiation-chemistry literature it is well known that ionizing radiation can cause different effects in clay minerals and their surrounding chemical environment (Allard et al. 2012). Severe mineral transformation such as radiation-induced amorphization could occur but has been shown to require relatively extreme doses on the order of several hundreds of kGy to MGy's. Lower doses comparable to the cumulative dose expected outside the copper canisters in the KBS-3 repository have however been shown to cause both short- and long-lived charge defects, such as electron holes detectable by electron paramagnetic resonance (EPR) in different clays. Furthermore, it is also known that radiation can induce redox processes involving the structural Fe (typically 3 weight% in bentonite Wyoming MX80) and affect the radiation chemical yield of radiolysis products in the clay associated water. Whereas the former two phenomena, mineral amorphization and generation of local charge defects have previously been studied and pose no threat to the overall functionality of the bentonite clay buffer, fundamental knowledge about the latter two processes is still lacking.

Regarding the clay buffers exposure to ionizing radiation, the initial dose rate will be dominated by gamma radiation. Figure 1 below from Håkansson, SKB report R-99-74 shows the estimated dose rate in mSv/h outside the copper canister holding BWR spent fuel at the burnup levels of 38 and 55 MWd/kg U, respectively. Integrating the dose rates from Håkansson, R-99-74 as well as from Cs-137 gamma radiation at different dose rates, results in the accumulated dose in Sv outside the copper canister shown in Figure 2.

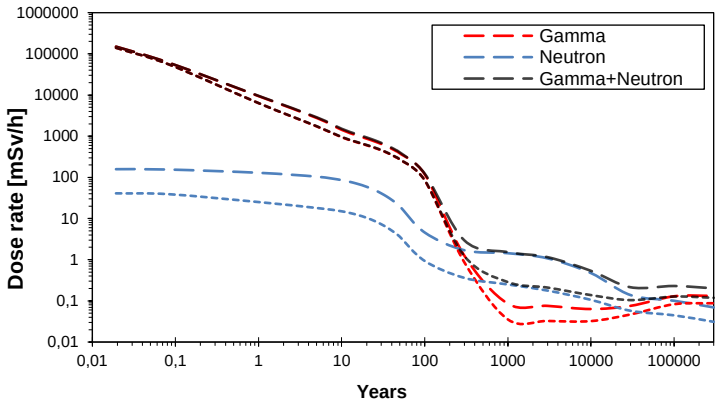

Figure 1. Estimated dose rate in mSv/h outside the copper canister from gamma and neutron radiation from BWR spent fuel with 38MWd/kg U (short dashes) and 55MWd/kg U (long dashes) burnup, respectively. Data taken from Håkansson, SKB Report R-99-74.

As can be seen in Figure 2, the total dose from gamma radiation drastically falls off after ca. 300 years, which coincides with the decay of Cs-137 (since 300 years corresponds to approx.10 times the half-lives). This is because Cs-137 dominates the gamma radiation after100 years. However, at shorter time scales other more short-lived fission products significantly contribute to the overall dose of gamma radiation.

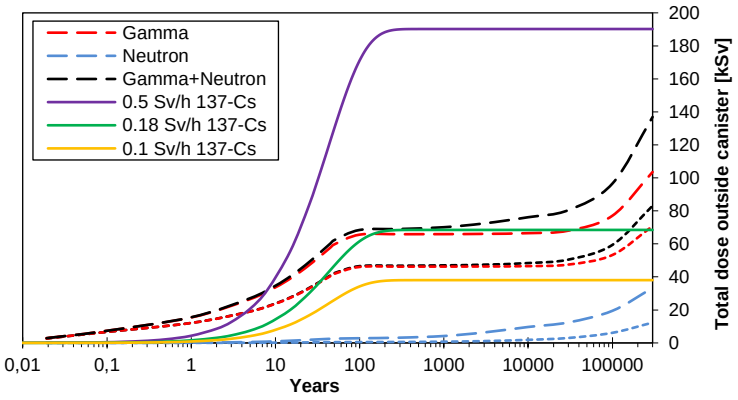

Figure 2. Accumulated dose in kSv outside the copper canister based on data in Figure 1 and burn-ups of 38 MWd/kg U (short dashes) and 55 MWd/kg U (long dashes), as well as the gamma radiation dose from Cs-137 assuming dose rates of 0.1, 0.18 and 0.5 Sv/h (solid lines).

Note that contrary to gamma photons, the quality factor (conversion factor from Sv to Gy) for neutrons is higher than 1 (typically 10), hence the actual amount of ionizing energy deposited by neutrons is significantly smaller (less than 1%) compared to the deposited ionizing energy of the gamma photons during the initial 100 years of repository after closure.

It is generally assumed that the total final dose from neutron and gamma radiation is on the order of 100 kSv. However as indicated by Figure 2 the actual total dose outside the spent fuel canisters will depend significantly on fuel burnup level and

reactor type. In fact, canisters with fuel from PWR reactors has been reported to show up to 50% higher initial dose rates compared to the same burnup in spent fuel from BWR reactors (Håkansson, SKB report R-99-74).

Figure 2 shows that a Cs-137 dose rate of 0.1 Sv/h represents a lower boundary in terms of gamma radiation which results in a total final and average dose of ca. 40 kSv. However, due to the geometry of the spent fuel insert and copper canister, the local maximum dose rate from a canister can be five times higher (Karnland 2004), resulting in a local final dose close to 200 kSv. A dose rate of 0.18 Sv/h Cs-137 agrees well with the upper average boundary of 55 MWd/kg U burnup spent fuel, resulting in a final gamma dose of approx. 70 kSv. Overall, Figure 2 also demonstrates that the major gamma dose results from the time-period after 10 years of repository operation, when the clay buffer is expected to be predominately anoxic and saturated with ground water.

The amount of ionizing radiation energy deposited in the clay buffer depends on the effective gamma radiation stopping power of the compacted and saturated bentonite. Since this relates to energy and mass, the unit Gray (Gy) is preferred over Sievert (Sv), since the former equals J/kg and hence can directly be used to quantify the amount of water radiolysis produced from a total dose using the so-called radiochemical yields (G, unit μmol/J), shown in Table 2 for gamma radiation (Spinks and Woods 1990).

Table 2. Radiochemical yield of the primary products from water radiolysis by γ-radiation.

Species	$e^-_{(aq)}$	$HO^\bullet$	H_3O^+	$G(H_2O_2)$	$H^\bullet$	H_2	$HO_2^\bullet$
G μmol/J	0.28	0.28	0.28	0.0725	0.062	0.0466	0.0027

For Cs-137 the gamma attenuation coefficients has been estimated to be 0.0861 cm^2/g and 0.0781 cm^2/g for water and dry bentonite, respectively, i.e. bentonites gamma stopping power is similar to that of water (Groenevelt 1974).

Assuming a fully saturated clay buffer of density 2000 kg/m^3 (SKB 2010) and a water porosity of 43%, an average attenuation coefficient for the saturated clay buffer becomes 0.0815 cm^2/g. Based on this an energy deposition profile can be obtained. Figure 3 shows the deposition of ionizing radiation in kGy, assuming an initial dose rate of 0.18 Gy/h of Cs-137.

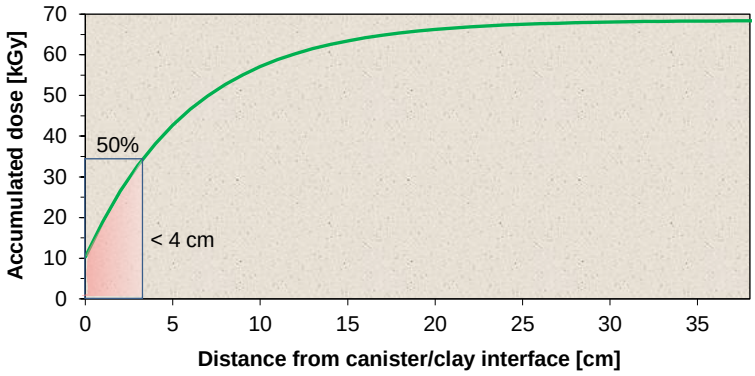

Figure 3. Accumulated dose in the clay buffer in kGy as a function of distance from the copper canister, for a buffer density of 2000 kg/m^3 and an initial dose rate of 0.18 Gy/h, corresponding to the green curve in Figure 2.

This profile shows that approx. 50% of the emitted gamma radiation energy will be deposited within the first 4 cm of the clay buffer from the copper canister/clay buffer interface. In fact only 0.3% of the gamma radiation would penetrate the entire clay buffer. This also means that any radiation-induced processes altering the native chemical properties of bentonite by for instance changing the redox state of the structural Fe(II) content, could possibly also affect the chemistry at copper canister interface, or influence redox chemistry of dissolved solutes such as sulphur species (HS^-/SO_4^{2-}) at the water/clay mineral interface.

In our previous research we have in recent years performed a series of studies investigating the radiation effects on bentonite. For practical reasons, these studies focusing on clay gels and clay suspensions have revealed that gamma irradiation can (*i)* enhance the colloidal stability of bentonite suspensions (Holmboe et al. 2009), (*ii)* alter the sorption capacity for certain radionuclides (Holmboe et al. 2011; Norrfors et al. 2017), as well as (*iii)* change the redox reactivity of the clay particles (Holmboe, Jonsson, and Wold 2012). The latter process is particularly interesting since it can be attributed to redox reactions of the structural Fe(II)/Fe(III) in montmorillonite lattice upon gamma irradiation, which from our previous experiments using montmorillonite clay suspensions (Figure 4) was shown to accelerate the decomposition of H_2O_2, due to direct or indirect reactions with the structural Fe(II). Most notably, these experiments demonstrated that gamma irradiation could increase the structural Fe(II)/Fe_{Tot} ratio from approx. ~3 to 30% under oxygen depleted conditions, using the 1,10-phenatroline method (Amonette and Templeton 1998).

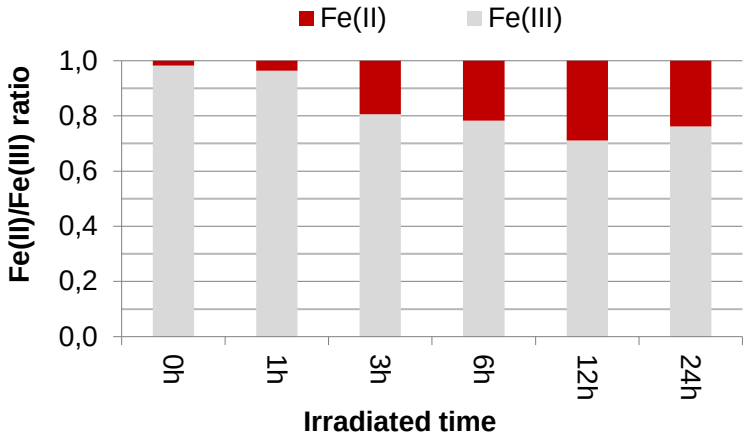

Figure 4. Radiation-induced increase in the structural Fe(II)/Fe(III) ratio as a function of irradiation time (24 h equals 13.3 kGy) as measured by the 1,10-phenatroline method, after irradiation of montmorillonite dispersions under anoxic conditions for a maximum of 24 h, corresponding to 13.3 kGy. Data from Holmboe et al., 2012.

For oxygenated montmorillonite suspensions, however, no apparent change in the structural Fe(II)-Fe(III) was found after the irradiations, indicating the strong reactivity of formed structural Fe(II) with dissolved oxygen and the possibility of forming even higher structural Fe(II)/Fe(III) ratios under completely oxygen free conditions, such as the compacted bentonite barrier in the KBS-3 repository a few years after closure.

Irradiations were also made in the presence of 5% 2-PrOH to scavenge and convert the hydroxyl radicals formed by water radiolysis to reducing α-hydroxyl-alkyl radicals, hence creating an overall reducing environment. As can be seen in Figure 5, an incomparable increase in the Fe(II)/Fe(III) ratio was observed. After 24 h or an equivalent of 13.3 kGy, the structural Fe(II)/Fe(III) ratio corresponded to 85%.

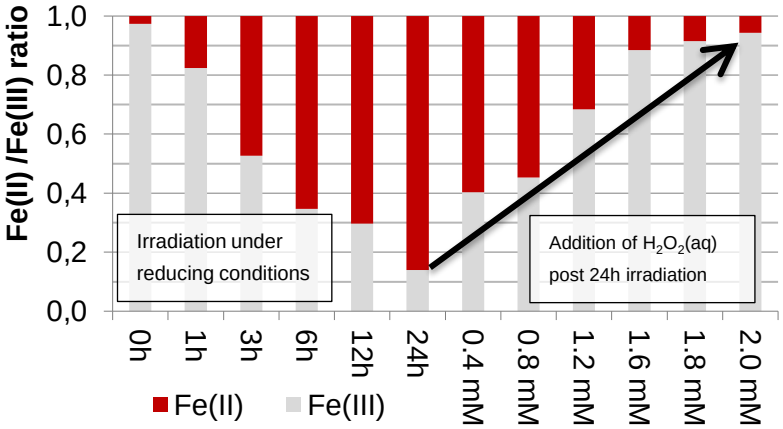

Figure 5. Radiation-induced increase in the structural Fe(II)/Fe(III) ratio as a function of irradiation time (24 h equals 13.3 kGy) in the presence of 2-PrOH, a hydroxyl radical scavenger. After irradiation for 24 h additions of H_2O_2(aq) were made, decreasing the structural Fe(II)/Fe(III) ratio. Data from Holmboe et al., 2012.

In similar samples irradiated for 24 h, post additions of H_2O_2(aq) was found to decrease the structural Fe(II)/Fe(III) ratio back to seemingly normal levels. Overall, this experiment highlighted the sensitivity of structural Fe to both reductants and oxidants, indicating that the redox state of structural Fe in the clay buffer may well be determined by the availability and balance between reductants and oxidants formed from water radiolysis.

The native montmorillonite in the common Wyoming bentonite MX80 (as reference bentonite) contain almost exclusively Fe(III) (approx. 97% of the total 3 weight%, see the first data column in Figure 4), hence the measured increase in structural Fe(II) relative to the structural Fe(III) suggests that the structural Fe_{Tot} could both be reduced and oxidized by the reactive and transient reducing and oxidizing species formed from water radiolysis (primarily e^-_{aq}, $H^\bullet$, $OH^\bullet$, H_2O_2). Such a process would in other words force the structural Fe_{Tot} to undergo constant back-and-forth redox-reactions between Fe(II) and Fe(III). Since elevated amounts of Fe(II) to the authors best knowledge is not naturally common in native montmorillonites, this 'flip-flopping' redox behaviour could hence probably cause significant lattice strain, and possibly cause additional structural charge defects over time. Since the montmorillonite lattice in typical reference bentonites such as Wyoming MX80 contains on average 0.3-0.4 Fe-atoms in the octahedral sheet and unit cell, or ca. 0.65-0.85 Fe per nm^2 (TR-06-30 2006; Holmboe 2011), a radiation-induced increase in the structural $Fe(II)/Fe_{Tot}$ ratio from 3 to 50% (the maximum $Fe(II)/Fe_{Tot}$ ratio found in previous experiments) would increase the surface charge density by almost 20%, from -0.11 C/m^2 to -0.141 C/m^2. Such radiation-induced change in the overall surface charge density would plausibly affect several physicochemical properties, such as swelling pressure, water uptake ability and the cation exchange capacity (CEC). Previously reported experiments utilizing chemical or microbial reduction of the structural Fe(III) has in fact demonstrated significant changes in several physical properties, such as the swelling pressure, CEC, total layer charge, specific surface area as well as microstructural properties (Khaled and Stucki 1991; Lear and Stucki 1987; Stucki et al. 1984; Lear and Stucki 1989; Stucki et al. 2003; Stucki and Tessier 1991; Plötze, Kahr, and Hermanns Stengele 2003), see also the review from POSIVA (POSIVA 2003).

Furthermore, apart from directly influencing the redox state of the structural Fe in the clay lattice, several studies have reported that irradiation of hydrated clays can significantly influence radiation chemical yield of the water radiolysis products and especially of H_2(g) in montmorillonite and other clays or cement materials (Eriksen, Christensen, and Bjergbakke 1987; Fattahi et al. 1992; Gournis et al. 2000; Plötze, Kahr, and Hermanns Stengele 2003; Fourdrin et al. 2013; Lainé et al. 2016; Lainé et al. 2017). Overall, the radiation induced production was found to depend on both mineral type as well as hydration state, and was by several studies reported to be dependent on transient trapping of electrons or hydrogen radicals or reactions within the clay lattice, where they would react with the existing structural Fe(II) or Fe(III) sites.

Surprisingly, there is a discrepancy in the reported state of the structural Fe (typically 3 wt% in total, mainly Fe(III)) and the Fe(II)/Fe(III) ratio of the reference clay MX80 bentonite. From previous research, the traditional 1,10-phenatroline wet-chemistry methods result in a low Fe(II)/Fe(III) ratio of approx. 3%. This is well in line with other reference smectite clay minerals available from the Clay Mineral Society and characterized in the so-called Base-line studies, since they show little to no structural Fe(II) in montmorillonite and similar clay minerals (www.clays.org/sourceclays_data/). However, in the XANES study conducted by the SKB AB and reported in Svensson et al 2013, the Fe(II)/Fe(III) of several water saturated reference clays (including MX80 bentonite) was reported to be much higher, with reports of astonishing 50% Fe(II)/Fe(III) under certain conditions. However, based on the reported photon flux at the MAX II synchrotron facility and experimental details from Svensson et al., 2013, these high Fe(II)/Fe(III) ratio has likely resulted from the Fe K-edge radiation exposure. To exemplify, with a photon flux **F** of $5x10^{11}$ photon/s (reported for beamline I811 at MAX II), a transmission factor **T** (here taken as 0.5, not known) and a photon energy **E** of 7112 eV (Fe K-edge), sample volume **V** of 0.25 mm^3 and measurement time **t** of 180 s (Svensson et al. 2013), the total sample dose can be estimated to be approx. 200 kGy.

$$\text{Dose} = F \times t \times T \times E \times 1.602 \times 10^{-19}/(V \times 10^{-6} \times 10^{3}) = 205 \text{ kGy}$$

This estimated sample dose is higher or on par with the gamma repository dose of 40-200 kGy in Figure 2, and could thus well explain the surprisingly high Fe(II)/Fe(III) ratio. This also indicates that synchrotron methods at for instance the new MAX IV facility (Lund, Sweden) which has an approx. tenfold higher photon flux than the previous MAX II facility, could be used to study induced radiation chemistry on-the-fly in future studies.

To investigate the effects of radiation-induced reduction of the structural Fe in montmorillonite, the aim of this study was to investigate if similar redox reactions involving the structural Fe would also occur in fully and partly saturated compacted bentonite clay, and elucidate the possible implications of elevated structural Fe(II) content for the physicochemical and redox chemical properties of bentonite under repository-like conditions.

The current study focused on the radiation-induced reduction of structural Fe(III) to Fe(II) in bentonite and montmorillonite clay samples as a function of gamma dose. This initial subtask is a direct continuation of our previously reported study using montmorillonite suspensions (Holmboe, 2012), albeit here with focus on irradiation of compacted clay pellets at controlled levels of saturation. Although we have already shown that gamma irradiation under anoxic conditions can significantly reduce the structural Fe(III) in montmorillonite suspensions, it is important to stress the need to elucidate the dependence of the water content for compacted clay samples. This is because the clay buffer will be partly water saturated upon installation (up to 65%, enough to cover all montmorillonite layer surfaces by almost two water layers), and be subjected to a temperature gradient from the copper

canister. Therefore, this subtask will use the methodology from Holmboe, 2011, irradiating compacted clay pellets water saturated under anoxic conditions in an inert atmosphere glove-box, incapsulated in closed PEEK plastic cells or glass ampules. As in our previous studies, the samples will be irradiated in a ^{137}Cs gamma source with a dose rate of 0.1 mGy/s for 0-3 days, corresponding to an accumulated dose of 0-26 kGy, comparable to the total gamma dose for the clay buffer in KBS-3 which is 40-200 kGy. The resulting structural and Fe(II) and Fe(III) contents will be analyzed by the standard 1,10-phenatroline method (Amonette and Templeton 1998).

In a second set of experiments, samples saturated and pre-equilibration with isotopically enriched deuterated ^{18}O water will be used (by mixing up to 10% $D_2{}^{18}O$ and 90% H_2O) and measured by IRMS, which is a isotope-ratio mass spectroscopy technique which allows for highly sensitive measurements of the isotope ratio of light gases such as $H_2(g)$ and $O_2(g)$. IRMS will be particularly useful for this project since it is well known that the lattice hydrogen atoms of the montmorillonite hydroxyl groups cannot easily undergo proton/deuterium exchange under ambient temperature conditions (Tournassat et al. 2004). Thus, any substantial change of the isotope ratios of H/D and $^{16}O/^{18}O$ due to the exposure to gamma irradiation compared to unirradiated reference samples, would be indicative of montmorillonite lattice alteration. After the irradiations of the clay samples (sealed glass ampules) measurements of the H/D and $^{16}O/^{18}O$ isotope ratios would be performed using IRMS at Umeå University (Shevela, Schröder, and Messinger 2018).

2. Materials and methods

2.1. Materials

The bentonite and montmorillonite clay materials, used in this study was Wyoming bentonite MX-80 (MX80) considered by SKB AB as their main reference bentonite. The MX80 mainly used in this study was supplied from the American Colloid Company via Prof. Mats Jonsson, Royal Institue of Technology (KTH), Stockholm, however a second batch of MX80 (MX80 2012 #14/Clun SKB) previously obtained from SKB AB was also tested for its Fe(II)/Fe(III) ratio. Since bentonite MX80 is a natural and mined material the montmorillonite composition, content, accessory minerals inventory and exchangeable counter-cations vary, but representative average values obtained and calculated from Karnland, SKB TR-06-30 are 82% montmorillonite and 74.8% Na^+,16.7% Ca^{2+}, 6.7% Mg^{2+} and 2% K^+ (TR-06-30 2006), see also Table 1 below. Apart from the different types of exchangeable counter-cations, the native and untreated MX80 also contains small amounts of Fe-containing minerals hematite, goethite, lepidocrocite, pyrite, magnetite, as well as organic residues. To avoid possible effects of mixed counter-cations, the accessory minerals and the organic residues, ion-exchanged and washed Ca^{2+}- and Na^+-montmorillonite materials (denoted NaMMT and CaMMT) was also used in the experiments. These pure clay materials were obtained by (i) removing organic residues by addition of 2M H_2O_2, and by (ii) ion-exchange through repeated washing with 0.5M NaCl(aq) or 0.1M $CaCl_2$(aq) solutions, respectively. This ion-exchange/washing procedure by centrifugation was repeated three times after which the clay dispersions were washed with de-ionized water until no precipitate formed in the supernatants after the addition of AgCl(aq). Furthermore, in order to test radiation induced effects on a more Fe-rich clay mineral, Nau-1 Nontronite from the Clay Mineral Society having approximately 22 wt% Fe (mainly replacing Al sites in the octahedral sheet of the clay lattice), was also used as received.

Table 1. Smectite unit cell compositions of bentonite MX80 and Nau-1 Nontronite(TR-06-30 2006; Keeling, Raven, and Gates 2000).

Bentonite MX80:	$M^+_{0.6}\left[Al_{3.11}Fe^{3+}_{0.37}Fe^{2+}_{0.01}Mg_{0.52}\right]\left[Si_{7.92}Al_{0.08}\right]O_{20}(OH)_4$
NAu-1:	$M^+_{1.0}\left[Fe^{3+}_{3.38}Mg_{0.05}Al_{0.58}\right]\left[Si_{7.00}Al_{1.00}\right]O_{20}(OH)_4$

2.2. Molecular dynamics simulations

The average d_{001} in a KBS-3 type clay buffer is approx. 17.7 Å and has a microstructure dominated by a 35%:65% mix of two-layered and three layered hydration states (in addition to a small amount of free interparticle porosity). In order to attain some atomistic insight into the behavior of the water radiolysis products $HO^\bullet$, $HOO^\bullet$ and H_2O_2 in such a nanoconfined and water saturated clay system, molecular dynamics (MD) simulations were performed of bilayered Na-montmorillonite systems corresponding to two-, three- and four-layer hydrate systems (denoted 2W,

3W, 4W), and having basal spacings (d_{001}) of 15.6, 18.9 and 21.8 Å as typically found experimentally (Holmboe, Wold, and Jonsson 2012), representing both higher and lower compactions than the bentonite clay buffer in KBS-3. Each simulation cell contained approx. 16200, 19800 and 22800 atoms (see Figure 7) with the full cell dimensions being approx. 42, 125, $2xd_{001}$ Ångström along the X, Y, Z directions. The clay layers had isomorphic substitution sites corresponding to 0.66/UC and were periodic along X but open in Y, by neutral AC-type edges (White and Zelazny 1988; Christophe Tournassat et al. 2016). The bulk pore ionic strength was set by 0.5M NaCl(aq), and the concentration of the $HO^{\bullet}$, $HOO^{\bullet}$ and H_2O_2 was set to approx. 20 mM. This high concentration was needed to assure adequate sampling statistics, since a sub-millimolar concentration effectively corresponds to less than one solute molecule per system, and hence could not be simulated without adhering to extremely large simulation cells.

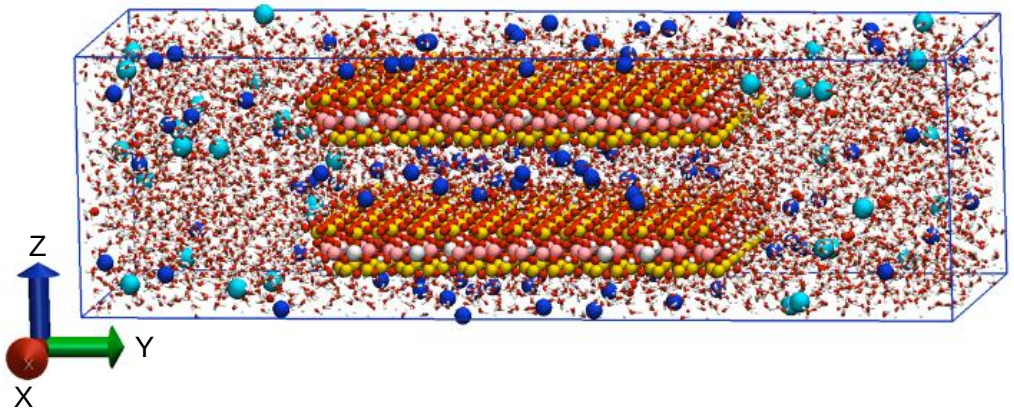

Figure 7. Example of and open bilayered simulation cell containing two Na-montmorillonite layers with neutral edges having a basal spacing of 18.9Å, corresponding to a three interlayer water layers (3W). Na^+ ions in blue, Cl^- in turquoise. Isomorphic substitution sites with Mg^{2+} shown as light gray in the octahedral and central sheet of the two clay layers.

After equilibration by energy minimization followed by 2 ns of volume and pressure optimization, production runs in NVT were performed for 500 ns using a 1 fs timestep. All simulations were carried out using GROMACS 2021, using a 1.0 nm cutoff for the direct van der Waals and for Coulombic interactions. Long-range Coulombic interactions were treated using the particle-mesh Ewald (PME) method. The clay layers with 0.66 octahedral substitutions per unit cell was modeled with CLAYFF with complete M-O angle terms to stabilize the clay edges (Cygan, Liang, and Kalinichev 2004; Holmboe 2019). Water simulated using the SPC/E model, with SPC/E compatible Na^+ and Cl^- ion-pair potentials and forcefield parameters for $HO^{\bullet}$, $HOO^{\bullet}$ and H_2O_2 species (Grigera, Berendsen, and TStraatsma 1987; Joung and Cheatham III 2009; Cordeiro 2014). Two separate trajectories were saved containing 5000 and 500000 configurations of water and non-water solutes, respectively, which was used to compute concentration 2D density maps and free energy profiles.

2.3. Gamma-irradiations

Two Cs-137 γ-sources producing 0.66 MeV gamma photons with a dose of approx. 0.1 Gy/s (KTH) or 0.013 Gy/s (Umeå University) was used for the gamma irradiations in this study. Prior the irradiations the clay samples were saturated with approx. equal weights of clay water and clay in a glove box under inert gas conditions in long NMR and Fe-free silicate test tubes. After a minimum of 1 day of equilibration the test tubes were capped, removed from the glove boxed and fused into shorter glass ampules under an open flame. The methodology of this critical step was repeated and improved upon several times during the cause of this study, due to the suspicion of trace amounts of O_2(g) affecting the induced radiation chemistry as found in previous studies. In fact, a significant fraction to the prepared glass ampules broke during the fusing step and was used as unirradiated reference samples. Figure 6 below shows representative of a saturated and irradiated ampule as well as a unirradiated reference ampule. The change in glass colour reflects the structural defects induced in the Fe-free glass silicate structure by the gamma irradiation.

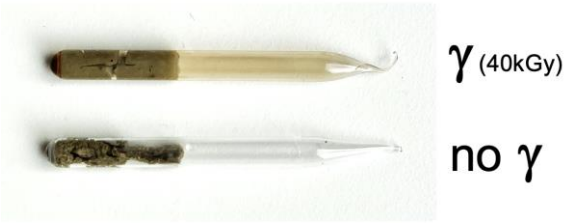

Figure 6. Photo of one glass ampule post 40 kGy irradiation and one unirradiated reference ampule.

Fe(II)/Fe(III) determination

The structural Fe(II)/Fe(III) ratio was analyzed using the 1,10- phenanthroline (phen) method described by Amonette and Templeton (1998). In this spectroscopic method the structural Fe(II) is analyzed after complete acid digestion by measuring the adsorption of the red Fe(II)-phen complex at 510 nm. Since the Fe(III)-phen complex is colorless, the total structural Fe and structural Fe(III) concentrations are obtained after complete reduction of any Fe(III) by hydroxylamine. In brief, approx. 50 mg of clay was added to a nearly boiling acid mixture consisting of 1:2:12 mL of HF (48 wt%):phen (10 wt% in EtOH): H_2SO_4 (10 wt%). After 30 min on 80 °C resulting in complete digestion, 10 mL of H_3BO_3 (5 wt%) and 90 mL of water were added to ensure long term stability of the resulting digestate. For the initial Fe(II) determination, 1 mL of the digestate was diluted with 10 mL of Na_3Cit(aq) (1 wt%) and measured at 510 nm. For the final total Fe determination, the digestate was first allowed to react for at least 60 min in 10 mL of Na_3Cit (1wt%) also containing 1 wt% NH_3OHCl, before measurement of the absorption at 510 nm.

2.4. Isotope ratio mass spectroscopy

In order to perform IRMS on gases evolving forming during the irradiation, clay samples were pre-equilibrated with either normal or 5wt%,10wt% or 30wt% addi-

tion of ^{18}O-/^{2}D-labeled water, respectively, thereafter the gas products were analyzed as a post analysis step by a time resolved IRMS setup as described previously (Melder et al. 2017). The setup consisted of a Delta V Plus IRMS instrument (Thermo Fischer Scientific), a cooling trap (−78 °C; dry ice + EtOH), and an in-house-built gas-tight membrane-inlet chamber with 200-µL working volume placed inside a glove box. Monitoring of H_2, O_2, and CO_2 was based on the *m/z* 2 ($^{1}H_2$), *m/z* 3 ($^{1}H^{2}D$), *m/z* 32 ($^{16}O_2$), *m/z* 34 ($^{16,18}O_2$), *m/z* 44 ($^{12}C^{16}O_2$), *m/z* 45 ($^{13}C^{16}O_2$) and *m/z* 46 ($^{12}C^{16,18}O_2$) signals.

3. Results and discussion

3.1. Molecular dynamics simulations

Studies based on molecular dynamics simulations (MD) investigating transient reactive species from water radiolysis or other radical generating processes are scarce, mainly because classical MD simulations per definition cannot handle breaking and formation of intramolecular bonds during a simulation. Nevertheless, MD simulations can be used to investigate the intermolecular interactions between ions and molecules, or as in this study mineral surface adsorption. Hence the trajectories from this study were used to compute 2D and 1D concentration maps and profiles, where the latter was used to obtain the free energy profiles, representing the free energy barrier for a solute between a water 'bulk' pore reservoir and a nanoconfined clay interlayer environment. This is because the Boltzmann factor can relate the Helmholtz free energy (ΔA, due to NVT simulations) to the interlayer and bulk pore concentrations according to Equation 1.

$$e^{-\Delta A(\xi)/k_B T} = \frac{C_\xi}{C_{bulk}} \qquad \textbf{Equation 1}$$

Here C_ξ is the solute concentration along the reaction coordinate ξ and C_{bulk} the bulk reservoir concentration outside the clay particle. ξ denotes the reaction coordinate, here taken as the Y-direction of the simulation cells. Hence a free energy barrier of 3 k_BT means that the probability or concentration of C_ξ is only ~5% of C_{bulk}. Note also that the ensemble kinetic potential of any molecular system results in a thermal energy of $\langle 3/2\ k_BT \rangle$.

A complete summary of all density maps for the 2W, 3W and 4W systems in the YX- and YZ- planes can be found in the Appendix and Figures S1-S10. Figure 7 shows representative 2D density maps of the concentrations [mol/L] of Na^+, Cl^-, $HO^\bullet$, $HOO^\bullet$ and H_2O_2 in the 3W hydrate system along the X-direction in the YZ-plane. In comparison to the cationic and anionic solutes, which are either concentrated (Na^+) due to charge balance reasons, or almost depleted (Cl^-) from the clay interlayers, the uncharged $HO^\bullet$, $HOO^\bullet$ and H_2O_2 solutes experience little influence of the clay interlayers, since they have similar concentrations in both types of pores. Figures S2, S4, S6, S8, S10 also indicated that they are only weakly affected by the heterogeneous surface charge density due to isomorphic substitution. However, by inspection of especially the 2W systems and by comparison of the surface densities of Na^+, $HO^\bullet$ and $HOO^\bullet$ (see the respective 2W states in Figures S2, S6 and S8), it is clear that $HO^\bullet$ and $HOO^\bullet$ radicals prefer less charged regions away from the isomorphic substitution sites and higher Na^+ density. Among H_2O_2, $HO^\bullet$ and $HOO^\bullet$, the latter two radicals also display quite similar behavior with a significant affinity to the neutral clay layer edges, and weak interlayer exclusion. H_2O_2 to a large extent resembles water (not shown), with little preference for either pore type.

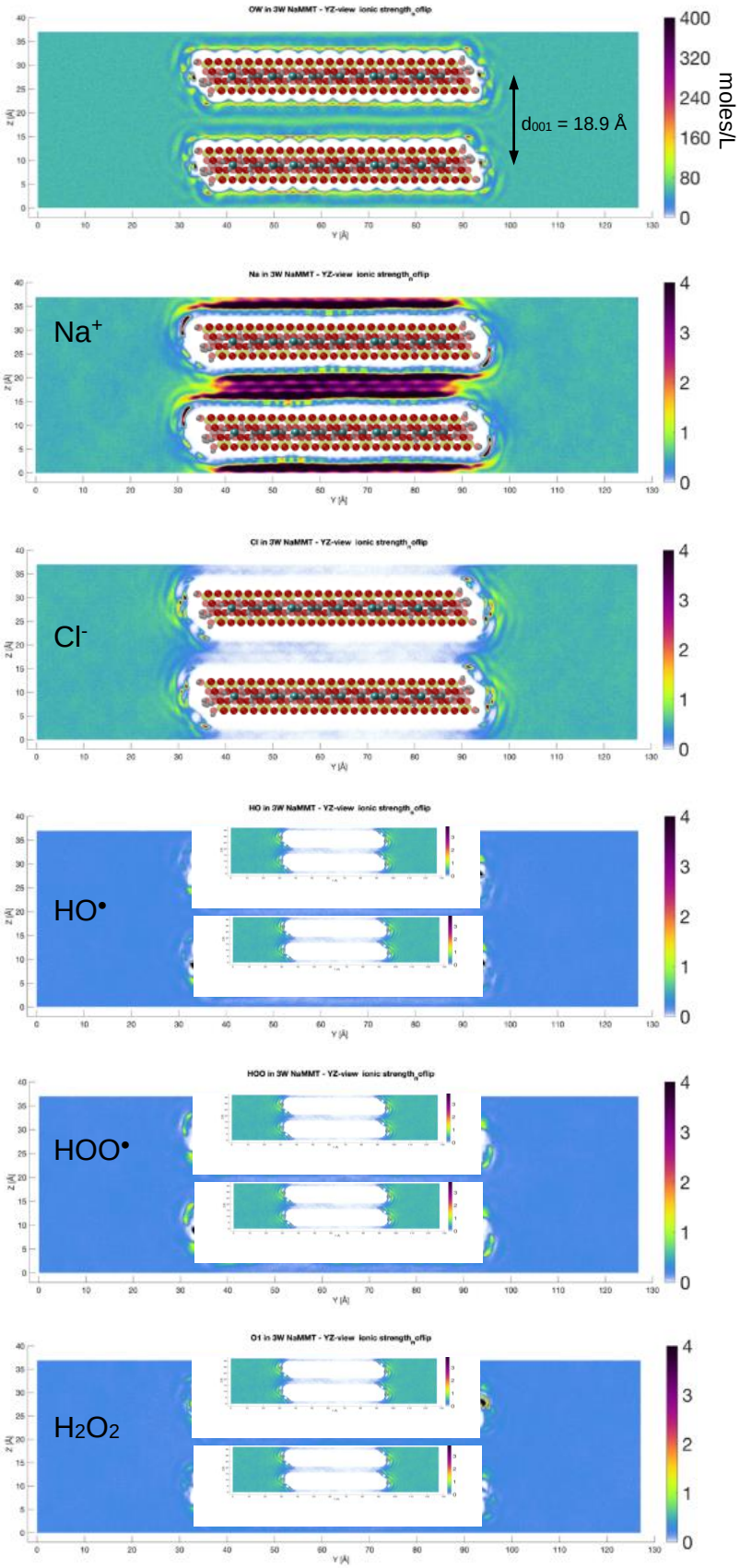

Figure 7. Collage of clay layers and 2D concentration maps of water-oxygen, Na^+, Cl^-, $HO^•$, $HOO^•$ and H_2O_2 in the 3W system (d_{001} 18.9 Å), shown along the X direction in the YZ-plane. Color bar on the right indicates concentrations in [moles/L].

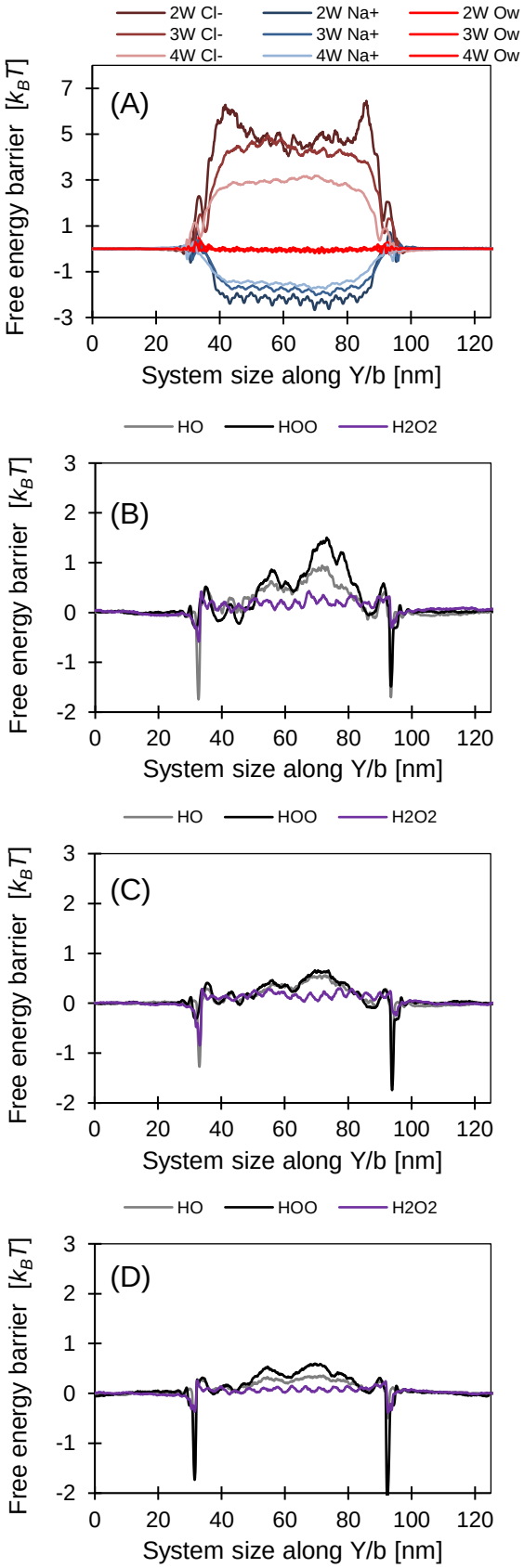

Figure 8. Free energy profiles of A) water-oxygen Ow, Na^+, Cl^-, and water-oxygen for the 2W, 3W and 4W states, B) $HO^\bullet$, $HOO^\bullet$ and H_2O_2 in the 2W system. C) $HO^\bullet$, $HOO^\bullet$ and H_2O_2 in the 3W system and $HO^\bullet$, $HOO^\bullet$ and H_2O_2 in the 4W system.

This resemblance among the $HO^{\bullet}$ and $HOO^{\bullet}$ radicals, and H_2O_2 to water, respectively, is also seen in the free energy profiles shown in Figure 8. In fact, both $HO^{\bullet}$ and $HOO^{\bullet}$ show similar free energy profile features and hence dependence on the surface charge heterogeneity (evident from Figure S2) created by the semi-random isomorphic substitution sites (obeying the Löwenstein's rule for Al^{3+}/Mg^{2+} replacement), which is less pronounced for H_2O_2 which shows similar interlayer density to water. Furthermore, the $HO^{\bullet}$ and $HOO^{\bullet}$ radicals show significantly greater affinity to the clay edges as evident from the approx. -1.5 k_BT to -2 k_BT energy minimum adjacent the clay edges, suggesting a 4 to 7 times of concentration factor of $HO^{\bullet}$ and $HOO^{\bullet}$ to the neutral clay edges. Nevertheless, the $HO^{\bullet}$ and $HOO^{\bullet}$ radicals and H_2O_2 experience lower free energy barriers for interlayer entry than the thermal $\langle 3/2\ k_BT \rangle$ limit for the 2W, 3W and 4W hydration states, hence experience relatively little exclusion from the interlayer regions in compacted bentonite.

Figure 9 also shows the sensitivity of anion exclusion of Cl^- for interlayer entry, which in previous studies has shown to be sensitive to ionic strength and interlayer pore size. Free energy barriers of this magnitude (compared to $\langle 3/2\ k_BT \rangle$) are however best estimated by even longer unconstrained simulations, or constrained simulations using for instance the umbrella sampling technique.

The differences in the free energy profile of Na^+ are almost entirely basal spacing and hence interlayer volume dependent, since the concentration of interlayer cations is foremost determined by the fixed clay layer charge. As can be seen water experiences little free energy barriers for interlayer entry, although some structuring adjacent to the clay layer edges exists, as also shown in Figure 7 (top).

3.2. Fe(II)/Fe(III) determination post gamma irradiation

In order to test if the structural Fe(II)/Fe(III) ratio change found in irradiated montmorillonite dispersions in our previous research also occurs for compacted and saturated clay preparations, gamma irradiations of four different clay materials: native Wyoming bentonite MX80, Na^+-exchanged MX80 (denoted NaMMT), Ca^{+2}-exchanged MX80 (denoted CaMMT), as well as the Fe-rich Nau-1 Nontronite. The results from three sets of irradiations corresponding to approx. 23.3, 40 and 60 kGy are presented here. The irradiations were performed under anoxic, oxic conditions as well as in the presence of 5% 2-PrOH in order to scavenge the main oxidant $HO^{\bullet}$, creating an excess of the reducing products from water radiolysis (see Table 2).

The structural Fe(II)/Fe(III) ratio from the Fe-rich (approx. 22 wt% Fe in total) Nau-1 Nontronite for both unirradiated samples and samples irradiated under anoxic or oxic conditions are shown in Figure 9A. The results from samples irradiated under predominately reducing conditions, in Figure 9B. The native Fe(II)/Fe(III) ratio for the unirradiated samples was 1.40% with a standard deviation of 0.12% (n=6), which assured the reproducibility of the method, even for such an Fe-rich clay mineral.

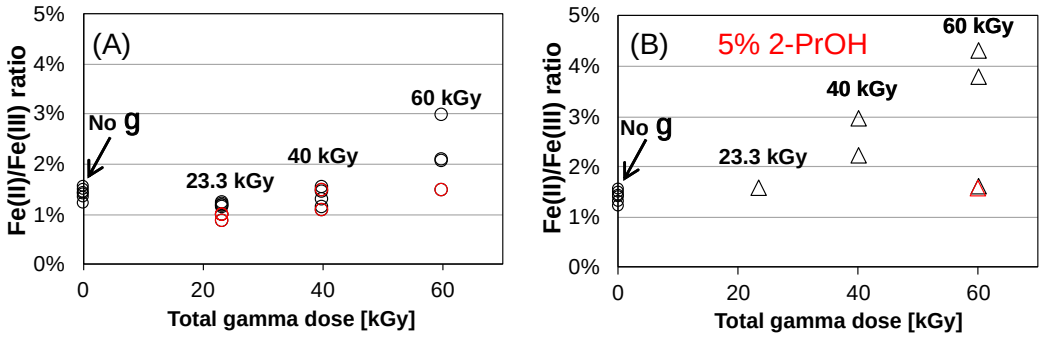

Figure 9. The Fe(II)/Fe(III) ratio in Nau-1 Nontronite as measured by the 1,10-phenantroline method using acid digestion for unirradiated (gray circles) and irradiated samples, under A) anoxic (brown) and oxic (red) conditions, B) overall reducing conditions due to the presence of excess 2-PrOH scavenging the HO• radical.

Figure 9 shows that for an Fe-rich smectite clay such as Nontronite, the relative increase in Fe(II)/Fe(III) ratio is small compared to previously found for montmorillonite, due to the approx. seven times higher Fe content in the clay. This indicates that the dose of ionizing radiation is the limiting factor. Although the number of data points are few, the general increase in Fe(II)/Fe(III) ratio with increasing dose further supports this conclusion. Overall, the samples irradiated under oxic conditions demonstrated no significant increase in the Fe(II)/Fe(III) ratio compared to the unirradiated samples.

The structural Fe(II)/Fe(III) ratio from the untreated reference bentonite MX80 (approx. 3 wt% Fe in total) for both unirradiated samples and samples irradiated under anoxic or oxic conditions are shown in Figure 10A. The native Fe(II)/Fe(III) ratio for two different batches of the unirradiated MX80 had 6.1%±0.23% Fe(II)/Fe(III) (MX80 from KTH) and 9.3%±0.48% (MX80 from SKB AB).

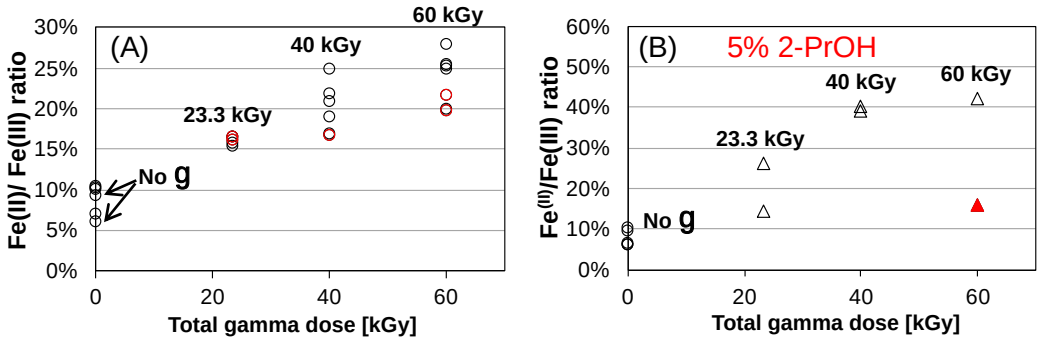

Figure 10. The Fe(II)/Fe(III) ratio in the untreated bentonite MX80 as measured by the 1,10-phenantroline method using acid digestion for unirradiated (black circles) and irradiated samples, under A) anoxic (gray) and oxic (red) conditions, B) overall reducing conditions due to the presence of excess 2-PrOH scavenging the HO• radical. Note the different scales in (A) and (B).

Figure 10 shows that for the more Fe-poor smectite clay material MX80 the relative increase in Fe(II)/Fe(III) ratio is rather significant compared to the Fe-rich Nau-1 Nontronite results, and in general in good agreement with what is previously found for montmorillonite dispersions in Figure 4. Overall, the Fe(II)/ Fe(III) ratio did increase with increasing total gamma dose for the anoxic samples. Interestingly, also the oxic samples displayed elevated Fe(II)/ Fe(III) ratios, albeit on the lower side compared to the anoxic samples (Figure 10A). Under predominately reducing conditions (Figure 10B), the Fe(II)/Fe(III) ratio in the anoxic samples reached an seemingly plateau at approx. 40% Fe(II)/ Fe(III), although this should be verified by further data, especially since an outlier at 23.3 kGy displayed little effect of the irradiations, possibly due to oxygen contamination.

The structural Fe(II)/Fe(III) ratio from the ion-exchanged and washed NaMMT (approx. 3wt% Fe in total, based on MX80 from KTH) for both unirradiated samples and samples irradiated under anoxic or oxic conditions are shown in Figure 11A. The Fe(II)/Fe(III) ratio for unirradiated NaMMT was 3.55%±0.32% and displayed similar albeit lower Fe(II)/Fe(III) ratios to the untreated MX80 (Figure 10A), with even oxic samples demonstrating increasing Fe(II)/Fe(III) levels. Under predominately reducing conditions (Figure 11B), the Fe(II)/Fe(III) ratio in one anoxic sample reached 50% Fe(II)/ Fe(III) after 60 kGy, however two samples at 40 kGy demonstrated only a small increase in Fe(II)/Fe(III) levels, possibly due to oxygen contamination. In line with Nau-1 and the untreated MX80, irradiation in the presence of 2-PrOH and oxygen resulted in very small increase in the Fe(II)/Fe(III) ratio.

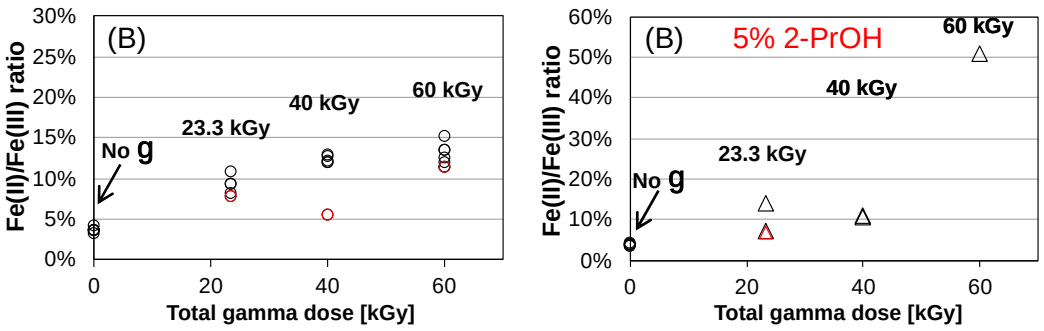

Figure 11. The Fe(II)/Fe(III) ratio in the untreated NaMMT as measured by the 1,10-phenantroline method using acid digestion for unirradiated (gray circles) and irradiated samples, under A) anoxic (blue) and oxic (red) conditions, B) overall reducing conditions due to the presence of excess 2-PrOH scavenging the $HO^{\bullet}$ radical. Note the different scales in (A) and (B).

For the ion-exchanged and washed CaMMT, the overall dependence on gamma irradiation appeared more similar to the untreated MX80 than NaMMT. However similar to NaMMT, the Fe(II)/Fe(III) ratio for unirradiated CaMMT was 3.30%±0.23% (Figure 10A). Similarly to MX80, anoxic samples of CaMMT showed more than 25% Fe(II)/Fe(III), albeit with a larger spread in the measured values. However even the known oxic samples demonstrated slightly increased Fe(II)/Fe(III) levels.

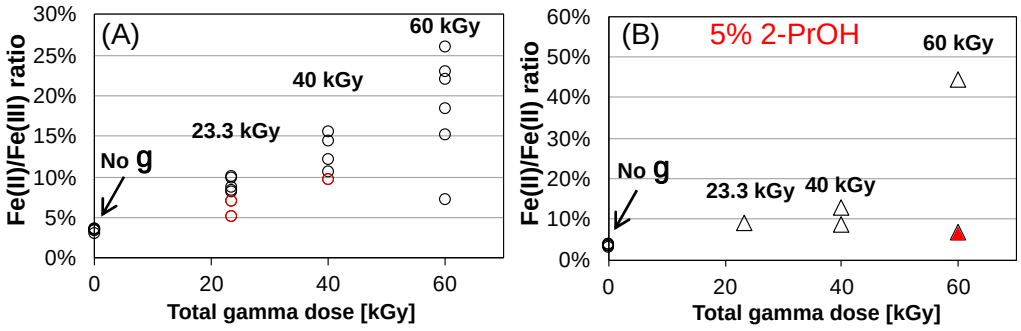

Figure 12. The Fe(II)/Fe(III) ratio in the untreated CaMMT as measured by the 1,10-phenantroline method using acid digestion for unirradiated (gray circles) and irradiated samples, under A) anoxic (green) and oxic (red) conditions, B) overall reducing conditions due to the presence of excess 2-PrOH scavenging the $HO^{\bullet}$ radical. Note the different scales in (A) and (B).

Under predominately reducing conditions (Figure 11B), the maximum Fe(II)/Fe(III) level was 44% at 60 kGy, however samples at 40 kGy demonstrated only a small increases in Fe(II)/Fe(III) levels, possibly due to oxygen contamination. In line with previous type of samples, irradiation in the presence of 2-PrOH and oxygen resulted in very small increase in the Fe(II)/Fe(III) ratio.

Overall, although large discrepancies in the measured data exist, possibly due to oxygen contamination during the sample preparation step, these results highlight the dependence in radiation induced effects on different clay materials as well as redox conditions. Furthermore, these results support findings from previous research using montmorillonite dispersions, by demonstrating a clear increase in the structural smectite Fe(II)/Fe(III) levels upon gamma irradiation.

3.3. Gas product evolution by gamma irradiation

Isotope ratio mass spectroscopy (IRMS) was used to probe the gas evolution in the clay samples due to 25.9 kGy of gamma irradition. IRMS cannot quantify gas formation directly but accurately measure the minute relative concentrations between gas isotopes. Hence NaMMT, CaMMT and MX80 clay samples were saturated with ^{18}O-/^{2}D-labeled water, and the effect of water decomposition and radiolysis for the different clay samples was probed by monitoring H_2(g) from the ratios of *m/z* 2 ($^{1}H_2$) and *m/z* 3 ($^{1}H^{2}D$) signals, O_2(g) from the ratios of the *m/z* 32 ($^{16}O_2$) and the *m/z* 34 ($^{16,18}O_2$) signals, and CO_2(g) from the ratios of *m/z* 44 ($^{12}C^{16}O_2$), *m/z* 45 ($^{13}C^{16}O_2$) and *m/z* 46 ($^{12}C^{16}O^{18}O$) signals.

Initial experimental attempts using small sample amounts and 5 wt% and 10 wt% of isotopically labeled water resulted in poor reproducibility. Hence here only the results from additions of isotopically labelled $H_2{}^{18}O$ (30 wt%) and $^{2}D_2O$ (30 wt%) water are presented in Figure 13 (H_2), Figure 14 (O_2), and Figure 15 (CO_2).

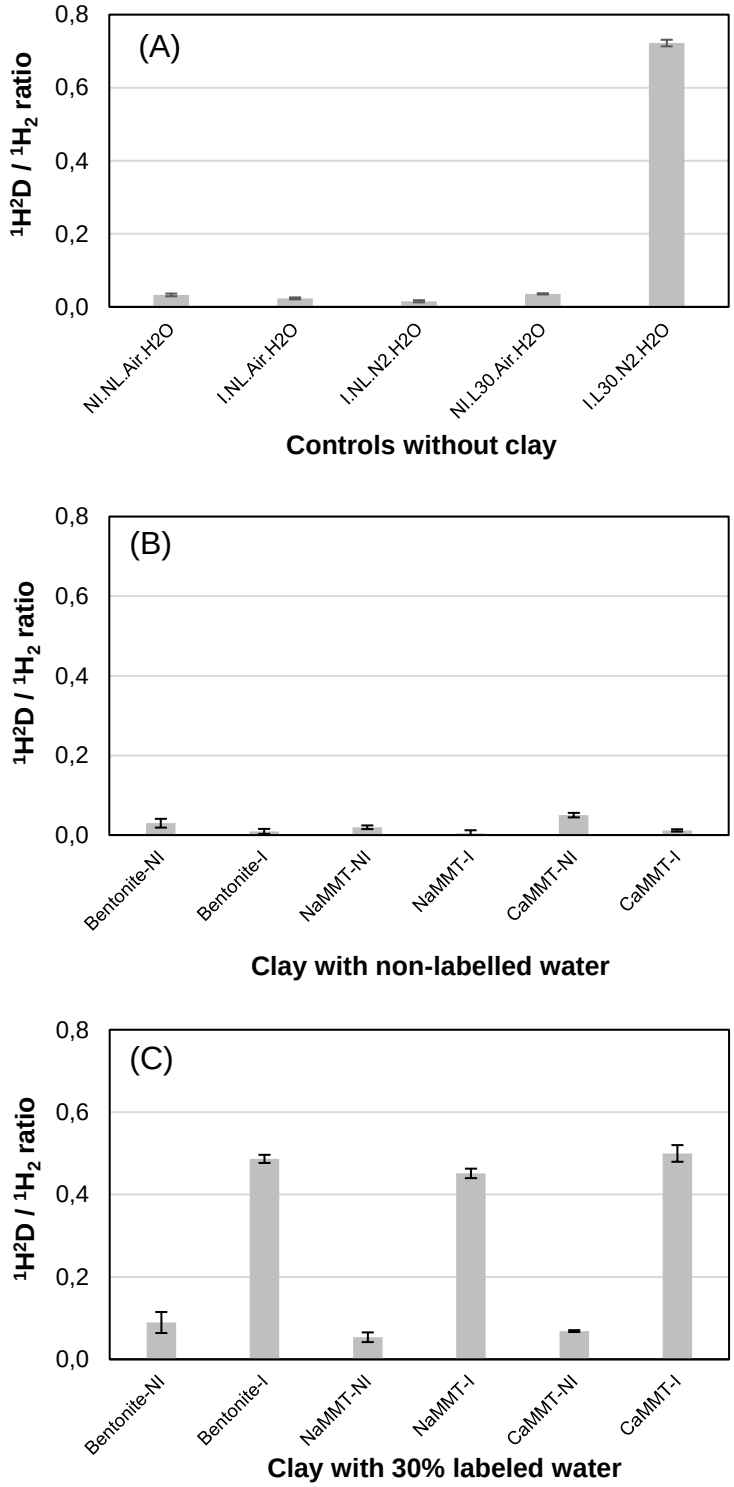

Figure 13. Gas products *m/z* ratios for $^1H^2D/^1H_2$ analyzed by IRMS. NI / I denote non-irradiated and irradiated samples, respectively. NL / L represent non-labelled an isotopically labelled water, respectively. (A) Control samples without clay. (B) Bentonite MX80, NaMMT and CaMMT clay samples saturated with normal non-labelled water. (C) Bentonite MX80, NaMMT and CaMMT clay samples saturated with normal 30 wt% labelled water.

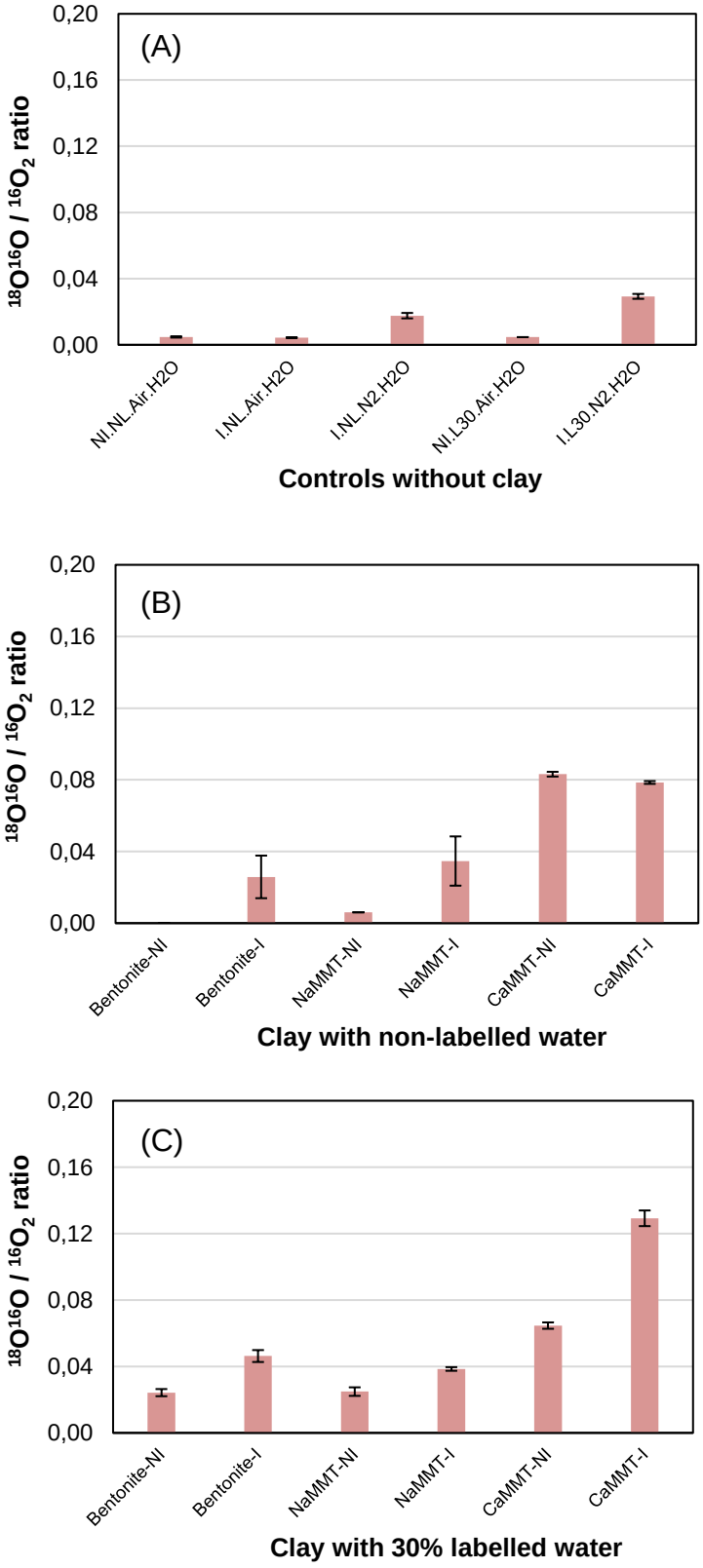

Figure 14. Gas products *m/z* ratios for $^{18}O^{16}O/^{16}O_2$ analyzed by IRMS. NI / I denote non-irradiated and irradiated samples, respectively. NL / L represent non-labelled an isotopically labelled water, respectively. (A) Controls samples without clay. (B) Bentonite MX80, NaMMT and CaMMT clay samples saturated with normal non-labelled water. (C) Bentonite MX80, NaMMT and CaMMT clay samples saturated with normal 30 wt% labelled water.

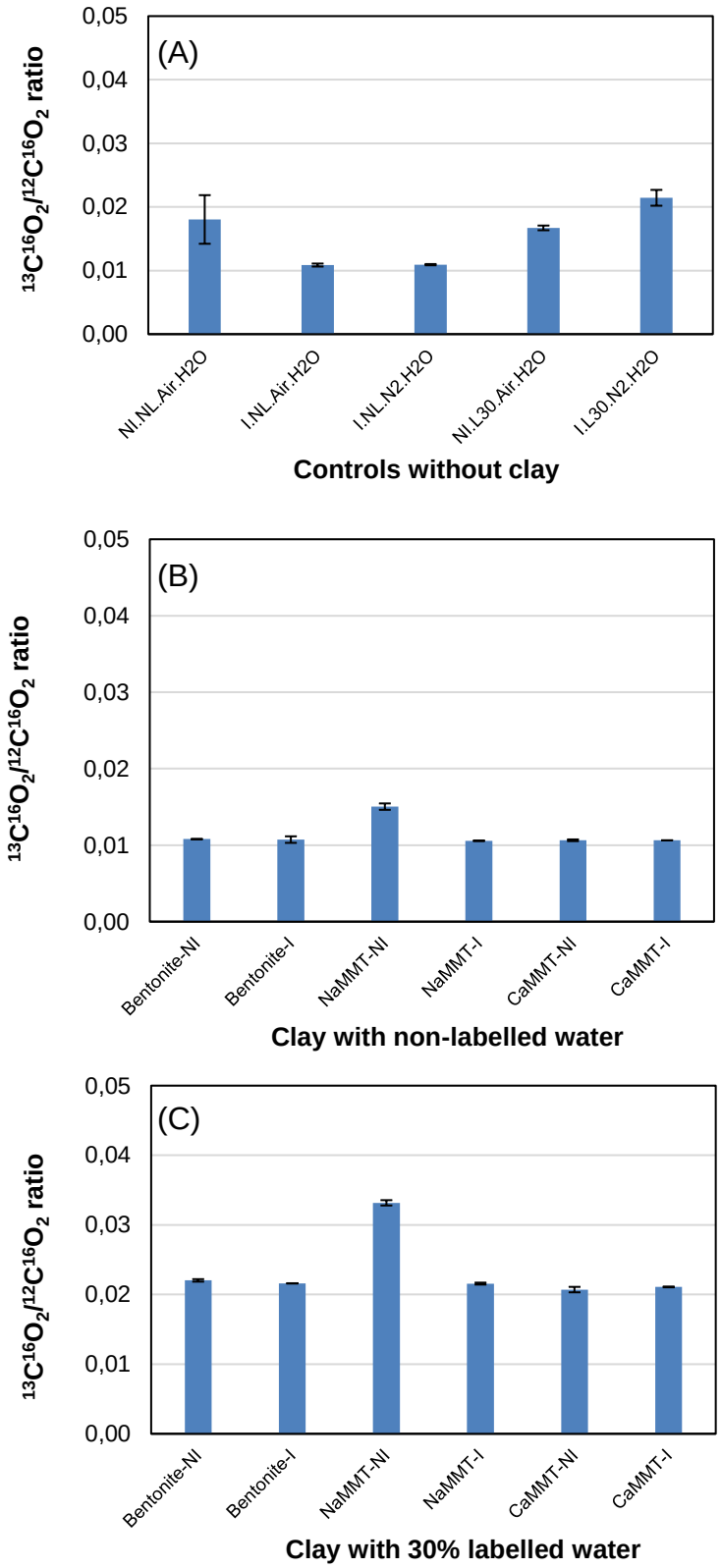

Figure 15. Gas products *m/z* ratios for $^{13}C^{16}O_2/^{12}C^{16}O_2$ analyzed by IRMS. NI / I denote non-irradiated and irradiated samples, respectively. NL / L represent non-labelled an isotopically labelled water, respectively. (A) Controls samples without clay. (B) Bentonite MX80, NaMMT and CaMMT clay samples saturated with normal non-labelled water. (C) Bentonite MX80, NaMMT and CaMMT clay samples saturated with normal 30 wt% labelled water.

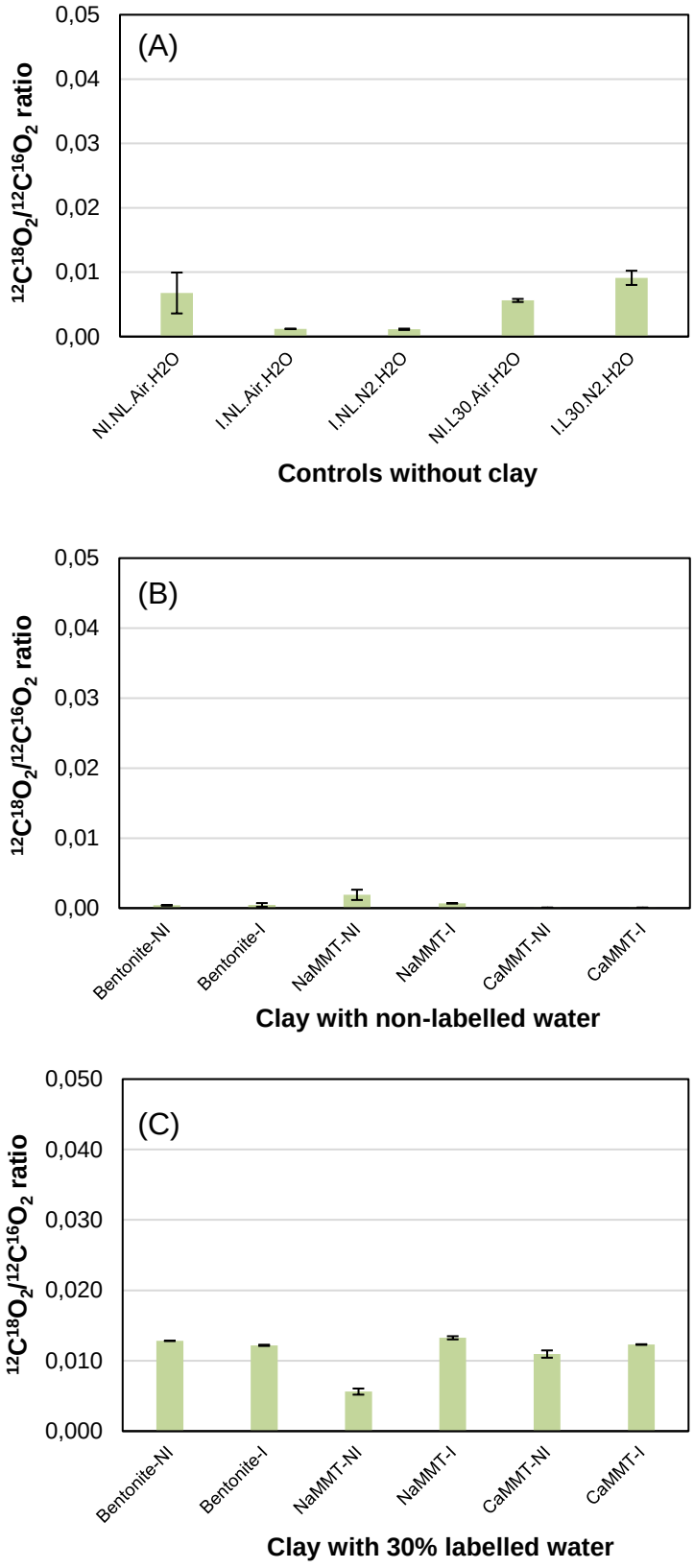

Figure 16. Gas products *m/z* ratios for $^{12}C^{18}O^{16}O/^{12}C^{16}O_2$ analyzed by IRMS. NI / I denote non-irradiated and irradiated samples, respectively. NL / L represent non-labelled an isotopically labelled water, respectively. (A) Controls samples without clay. (B) Bentonite MX80, NaMMT and CaMMT clay samples saturated with normal non-labelled water. (C) Bentonite MX80, NaMMT and CaMMT clay samples saturated with normal 30 wt% labelled water.

As can be seen in Figure 13 for the control samples without clay, irradiated samples saturated with non-labelled and regular water (H_2O) had very low $^1H^2D/^1H_2$ ratios due to the absence of D addition. Non-irradiated samples saturated with 30wt% labelled water (D_2O) and not subjected to hydrogen gas evolution due to irradiation also displayed low $^1H^2D/^1H_2$ ratios. However, for the irradiated sample containing labeled water, the $^1H^2D/^1H_2$ ratio was 0.722±0.009. This can be compared to the theoretical maximum $^1H^2D/^1H_2$ mixing ratio of 0.857 for a 30wt% labeled D_2O solution, since at equilibrium it would contain 49% H_2O, 42% HDO and 9% D_2O (Katsir et al. 2010). The discrepancy between the measured $^1H^2D/^1H_2$ ratio and theoretical mixing ratio could possibly be attributed to the differences in radiochemical yields between H_2O and D_2O systems, which has been reported to significantly differ for several radiolytic products. In fact, $G(D_2)$ has been reported to be approx. 20% lower than $G(H_2)$, and $G(D)+ G(D_2)$ 33% lower than $G(H)+ G(H_2)$ (Elliot, Chenier, and Ouellette 1993; Swiatla-Wojcik and Buxton 2001). Due to this and to the fact that radiochemical yields of mixed D_2O/H_2O systems are lacking in the literature, it is difficult to accurately quantify the production of hydrogen gas from these mixed H_2O, HDO and D_2O systems.

Nevertheless, for the irradiated (I) samples containing clay shown in Figure 13C the MX80, NaMMT and CaMMT samples all produced lower $^1H^2D/^1H_2$ ratios of 0.45-0.50, regardless of counter-cation and smectite clay material. Theoretically, $^1H^2D/^1H_2$ ratios of 0.722 and approx. 0.50 for the control and clay samples respectively, would correspond to 26.5% to approx. 20% labelled D_2O water, respectively. Hence, the irradiated clay samples indicate a significant dilution of ^2D on behalf of ^1H, possibly due to different direct radiochemical yields in the heterogeneous systems containing clay, or indirectly due to reactions and abstraction of the clay lattice or edge H-sites.

For the case of O_2 the theoretical maximum $^{18}O^{16}O/^{16}O_2$ mixing ratio with the labelled water is also 0.857. For the control samples without clay and samples saturated with non-labelled normal water, the detected $^{18}O^{16}O/^{16}O_2$ ratios were also low albeit frequently higher for the irradiated samples compared to the unirradiated samples, especially in the case of labelled water, Figure 14C. Different to the case of H_2, CaMMT produced almost a factor of two higher $^{18}O^{16}O/^{16}O_2$ mixing ratios compared to NaMMT and the untreated MX80, but not only for the irradiated samples but also for the non-irradiated samples.

For the case of CO_2 the theoretical maximum $^{13}C^{16}O^{16}O/^{12}C^{16}O_2$ (Figure 15) and the $^{12}C^{18}O^{16}O/^{12}C^{16}O_2$ (Figure 16) mixing ratios are 0.0118 and 0.857, respectively. Since the statistical accuracy increases with increasing theoretical mixing ratio, the latter case with $^{12}C^{18}O^{16}O$ would represent more reliable data. In view of this the data of $^{13}C^{16}O^{16}O/^{12}C^{16}O_2$ in Figure 15 seemingly display higher mixing ratios than physically possible for the case of labelled water. Interestingly for both cases of CO_2 data, no significant effect of irradiation was found regardless of sample type compared to the corresponding non-irradiated samples.

Overall, the results from the detection of $^{1}H^{2}D$ show evidence of significant gas formation induced by gamma radiation, in line with findings from previous studies in the literature mentioned in the introduction. This is to a lesser extent also supported by the production of $^{18}O^{16}O$, but not $^{13}C^{16}O^{16}O/^{16}O_2$ or $^{12}C^{18}O^{16}O/^{12}C^{16}O_2$.

Due to concern regarding oxygen contamination during the sample preparations, direct $O_2(g)$ measurements were also made in addition to the IRMS measurements. Based on a subset of 8 prepared ampules containing saturated clay samples, an oxygen content of 3.07±0.56% was found. Such a significant oxygen level, being present either initially or being formed during the gamma irradiation could obviously contribute to the erratic outliers found in the Fe(II)/Fe(III) ratio data, as well as have influenced the presented IRMS results, and ideally should be investigated further.

4. Summary

The current study investigated the effects of gamma radiation and water radiolysis on saturated bentonite MX80, Na^+ and Ca^{2+} ion-exchanged montmorillonite as well as an Fe-rich smectite, Nau-1 Nontronite.

- Molecular dynamics simulations were initially performed to investigate the behaviour of the water radiolysis products H_2O_2, $HO^\bullet$ and $HOO^\bullet$ to give atomistic insight into the behavior and surface affinity of these water radiolysis products adjacent to hydrated smectite surfaces, and in particular the interlayer regions. The results show that H_2O_2, $HO^\bullet$ and $HOO^\bullet$ are neither strongly interacting nor strongly excluded from the interlayer regions, although the latter two radicals showed some preference to surface regions avoid of isomorphic substitution sites and high density of counter-cations. The same species also showed significant affinity to the neutral clay edges modelled.
- Investigation of changes in the (structural) Fe(II)/Fe(III) levels due to exposure to gamma irradiation in general agreed with prior experiments obtained using clay dispersions, and generally showed that Fe(II) levels increase in place of Fe(III) with increasing gamma dose. This supports the hypothesis that ionizing radiation can both reduce and oxidize (flip-flop) structural Fe via water radiolysis. Depending on the experimental conditions Fe(II)/Fe(III) ratios of up to 25%-30% under anoxic conditions and 40%-50% under strictly reducing conditions were found. Poor reproducibility in the measured Fe(II)/Fe(III) levels of the irradiated samples were however indicative of oxygen contamination in a significant fraction of the measured samples.
- The gas formation of H_2, O_2 and CO_2 was investigated by means of IRMS, using isotopically labelled and non-labelled water. The results from measurements of $^1H^2D/^1H_2$ ratios show evidence of significant gas formation induced by gamma radiation, in line with findings from previous studies in the literature. Interestingly this indirect evidence of radiation chemistry involving hydrogen gas was insensitive to the investigated clay sample type. Analysis of $O_2(g)$ in a subset of the prepared samples however revealed significant trace levels of oxygen. The effect of such high levels of oxygen present potentially pre-irradiation should further be investigated before drawing further conclusions regarding the gas formation of O_2 and CO_2.

5. Outlook

The results of this study confirm previous reports that gamma irradiation under anoxic conditions reduces Fe(III) to Fe(II) in smectite clay minerals and increases radiochemical yields of hydrogen. However, this study also revealed practical difficulties with the methodology used and highlighted limitations in investigating the radiation chemistry of heterogeneous and complex geochemical systems. To overcome some of these hurdles, new synchrotron-based experiments should be undertaken. Such experiments would not only allow for on-the-fly irradiation and characterization due to the high flux rates and brilliance at modern synchrotron facilities but also resolve the existing discrepancy in measured Fe(II)/Fe(III) levels between traditional wet chemistry methods (as used in the current study) and prior synchrotron studies that did not take radiation chemical effects into consideration.

6. References

Allard, Th, E. Balan, G. Calas, C. Fourdrin, E. Morichon, and S. Sorieul. 2012. "Radiation-Induced Defects in Clay Minerals: A Review." *Nuclear Instruments and Methods in Physics Research, Section B: Beam Interactions with Materials and Atoms* 277: 112–20. https://doi.org/10.1016/j.nimb.2011.12.044.

Amonette, J E, and J C Templeton. 1998. "Improvements to the Quantitative Assay of Nonrefractory Minerals for Fe(II) and Total Fe Using 1,10-Phenanthroline." *Clays and Clay Minerals* 46 (1): 51–62.

Cordeiro, Rodrigo M. 2014. "Reactive Oxygen Species at Phospholipid Bilayers: Distribution, Mobility and Permeation." *Biochimica et Biophysica Acta - Biomembranes* 1838 (1 PARTB): 438–44. https://doi.org/10.1016/j.bbamem.2013.09.016.

Cygan, Randall T., Jian-Jie Jie Liang, and Andrey G. Kalinichev. 2004. "Molecular Models of Hydroxide, Oxyhydroxide, and Clay Phases and the Development of a General Force Field." *Journal of Physical Chemistry B* 108 (4): 1255–66. https://doi.org/10.1021/jp0363287.

Elliot, A John, Monique P Chenier, and Denis C Ouellette. 1993. "H,o d,O" 89 (8): 1193–97.

Eriksen, T. E., H. Christensen, and E. Bjergbakke. 1987. "Hydrogen Production in α-Irradiated Bentonite." *Journal of Radioanalytical and Nuclear Chemistry Articles* 116 (1): 13–25. https://doi.org/10.1007/BF02037207.

Fattahi, M., C. Houée-Levin, C. Ferradini, and P. Jacquier. 1992. "Hydrogen Peroxide Formation and Decay in γ-Irradiated Clay Water." *International Journal of Radiation Applications and Instrumentation. Part* 40 (3): 167–73. https://doi.org/10.1016/1359-0197(92)90019-C.

Fourdrin, C., H. Aarrachi, C. Latrille, S. Esnouf, F. Bergaya, and S. Le Caër. 2013. "Water Radiolysis in Exchanged-Montmorillonites: The H2 Production Mechanisms." *Environmental Science and Technology* 47 (16): 9530–37. https://doi.org/10.1021/es401490t.

Gournis, D., A. E. Mantaka-Marketou, M. A. Karakassides, and D. Petridis. 2000. "Effect of γ-Irradiation on Clays and Organoclays: A Mossbauer and XRD Study." *Physics and Chemistry of Minerals* 27 (7): 514–21. https://doi.org/10.1007/s002690000089.

Grigera, J.R, H.J.C. Berendsen, and T.P Straatsma. 1987. "The Missing Term in Effective Pair Potentials." *Journal of Physical Chemistry* 91: 6269–71.

Groenevelt, P. H. 1974. "The Use of a Dual Gamma Scanner to Observe the Shrinkage of Clay." *Geoderma* 11 (4): 287–95. https://doi.org/10.1016/0016-7061(74)90055-X.

Holmboe, M., M. Jonsson, and S. Wold. 2012. "Influence of γ-Radiation on the Reactivity of Montmorillonite towards H2O2." *Radiation Physics and Chemistry* 81 (2). https://doi.org/10.1016/j.radphyschem.2011.10.009.

Holmboe, M., K. Karin Norrfors, M. Jonsson, and S. Wold. 2011. "Effect of γ-Radiation on Radionuclide Retention in Compacted Bentonite." *Radiation Physics and Chemistry* 80 (12). https://doi.org/10.1016/j.radphyschem.2011.08.004.

Holmboe, Michael. 2019. “Atom: A MATLAB PACKAGE FOR MANIPULATION OF MOLECULAR SYSTEMS.” *Clays and Clay Minerals* 67 (5): 419–26. https://doi.org/10.1007/s42860-019-00043-y.
Holmboe, Michael. 2011. *The Bentonite Barrier: Microstructural Properties and Influence of γ-Radiation*. *Doctoral Thesis*.
Holmboe, Michael, Susanna Wold, and Mats Jonsson. 2012. “Porosity Investigation of Compacted Bentonite Using XRD Profile Modeling.” *Journal of Contaminant Hydrology* 128 (1–4): 19–32. https://doi.org/10.1016/j.jconhyd.2011.10.005.
Holmboe, Michael, Susanna Wold, Mats Jonsson, S Garcia-Garcia, and Sandra García-García. 2009. “Effects of γ-Irradiation on the Stability of Colloidal Na+-Montmorillonite Dispersions.” *Applied Clay Science* 43 (1): 86–90. https://doi.org/10.1016/j.clay.2008.07.004.
Joung, In Suk, and Thomas E. Cheatham III. 2009. “Halide Ions Using Water-Model-Specific Ion Parameters.” *Journal of Physical Chemistry B* 113 (40): 13279–90. https://doi.org/10.1108/SHR-03-2018-0019.
Karnland, Ola. 2004. “TR-04-06, Final Disposal of Fuel – Electron Radiation Outside Copper Canister.” *SKB Technical Report TR-04-06*.
Katsir, Yael, Yoash Shapira, Yitzhak Mastai, Rumiana Dimova, and Eshel Ben-Jacob. 2010. “Entropic Effects and Slow Kinetics Revealed in Titrations of D 2 O−H 2 O Solutions with Different D/H Ratios.” *The Journal of Physical Chemistry B* 114 (17): 5755–63. https://doi.org/10.1021/jp909657m.
Keeling, John L, Mark D Raven, and Will P Gates. 2000. “Geology and Characterization of Two Hydrothermal Nontronites from Weathered Metamorphic Rocks at the Uley Graphite Mine, South Australia.” *Clays and Clay Minerals* 48 (5): 537–48.
Khaled, E M, and J W Stucki. 1991. “Iron Oxidation State Effects on Cation Fixation in Smectites.” *Soil Sci. Soc. Am. J* 55: 550–54.
Lainé, M., E. Balan, T. Allard, E. Paineau, P. Jeunesse, M. Mostafavi, J. L. Robert, and S. Le Caër. 2017. “Reaction Mechanisms in Swelling Clays under Ionizing Radiation: Influence of the Water Amount and of the Nature of the Clay Mineral.” *RSC Advances* 7 (1): 526–34. https://doi.org/10.1039/c6ra24861f.
Lainé, Maxime, Thierry Allard, Etienne Balan, François Martin, H. Jurgen Von Bardeleben, Jean Louis Robert, and Sophie Le Caër. 2016. “Reaction Mechanisms in Talc under Ionizing Radiation: Evidence of a High Stability of H• Atoms.” *Journal of Physical Chemistry C* 120 (4): 2087–95. https://doi.org/10.1021/acs.jpcc.5b11396.
Lear, P. R., and J. W. JW Stucki. 1989. “Effects of Iron Oxidation State on the Specific Surface Area of Nontronite.” *Clays & Clay Minerals* 37 (6): 547–52. https://doi.org/10.1346/CCMN.1989.0370607.
Lear, P R, and J W Stucki. 1987. “Intervalence Electron Transfer and Magnetic Exchange in Reduced Nontronite.” *Clays and Clay Minerals* 35 (5): 373–78.
Melder, Jens, Wai Ling Kwong, Dmitriy Shevela, Johannes Messinger, and Philipp Kurz. 2017. “Electrocatalytic Water Oxidation by MnO x /C: In Situ Catalyst Formation, Carbon Substrate Variations, and Direct O 2 /CO 2 Monitoring by Membrane-Inlet Mass Spectrometry.” *ChemSusChem* 10 (22):

4491–4502. https://doi.org/10.1002/cssc.201701383.
Norrfors, K Karin, Åsa Björkbacka, Amanda Kessler, Susanna Wold, and Mats Jonsson. 2017. “γ -Radiation Induced Corrosion of Copper in Bentonite-Water Systems under Anaerobic Conditions.” *Radiation Physics and Chemistry* 144 (November): 8–12. https://doi.org/10.1016/j.radphyschem.2017.11.004.
Plötze, M., G. Kahr, and R. Hermanns Stengele. 2003. “Alteration of Clay Minerals - Gamma-Irradiation Effects on Physicochemical Properties.” *Applied Clay Science* 23 (1–4): 195–202. https://doi.org/10.1016/S0169-1317(03)00103-0.
POSIVA. 2003. “Bentonite Iron Interactions in Natural Occurrences and in Laboratory The Effects of the Interactions on the Propertiees of Bentonites a Literature Survey.” *Working Report 2003-55*, no. October.
R-99-74, and R Håkansson. 1999. “Beräkning Av Nuklidinnehåll, Resteffekt, Aktivitet Samt Doshastighet För Utbränt Kärnbränsle.” *SKB Technical Report* R-99-74.
Shevela, Dmitriy, Wolfgang P. Schröder, and Johannes Messinger. 2018. “Liquid-Phase Measurements of Photosynthetic Oxygen Evolution.” In *Photosynthesis: Methods and Protocols, Methods in Molecular Biology*, 1770:197–211. University of Arkansas Press. https://doi.org/10.1007/978-1-4939-7786-4_11.
SKB. 2010. “Design, Production and Initial State of the Buffer. SKB TR-10-15.” *TR-10-15*. www.skb.se.
Spinks, J.W.T., and R.J. Woods. 1990. *Water and Inorganic Aqueous Systems. Introduction to Radiation Chemistry*. John Wiley and Sons Inc.
SSM. 2018. *Strålsäkerhet Efter Slutförvarets Förslutning. Report No. 2018:07*.
Stucki, J W, P F Low, C B Roth, and D C Golden. 1984. “Effects of Oxidation State of Octahedral Iron on Clay Swelling.” *Clays and Clay Minerals* 32 (5): 357–62. https://doi.org/10.1346/CCMN.1984.0320503.
Stucki, J W, and D Tessier. 1991. “Effects of Iron Oxidation State on the Texture and Structural Order of Na-Nontronite Gels.” *Clays and Clay Minerals* 39 (2): 137–43.
Stucki, Joseph W., Kangwon Lee, Lingzhi Zhang, and Richard A. Larson. 2003. “Effects of Iron Oxidation State on the Surface and Structural Properties of Smectites.” *Pure and Applied Chemistry* 74 (11): 2145–58. https://doi.org/10.1351/pac200274112145.
Swiatla-Wojcik, D., and G. V. Buxton. 2001. “Isotopic Effect in the Radiolysis of Water. Diffusion-Kinetic Modelling up to 300°C.” *Research on Chemical Intermediates* 27 (7–8): 875–89. https://doi.org/10.1163/15685670152622149.
Tournassat, C, E Ferrage, C Poinsignon, and L Charlet. 2004. “The Titration of Clay Minerals: II. Structure-Based Model and Implications for Clay Reactivity.” *Journal of Colloid and Interface Science* 273 (1): 234–46.
Tournassat, Christophe, I.C. Ian C. Bourg, Michael Holmboe, Garrison Sposito, and Carl I. C.I. Carl I. Steefel. 2016. “Molecular Dynamics Simulations of Anion Exclusion in Clay Interlayer Nanopores.” *Clays and Clay Minerals* 64 (4): 374–88. https://doi.org/10.1346/CCMN.2016.0640403.

TR-06-09. 2006. “Long-Term Safety for KBS-3 Repositories at Forsmark and Laxemar – a First Evaluation Main Report of the SR-Can Project.” *SKB Technical Report*.
TR-06-30. 2006. “Mineralogy and Sealing Properties of Various Bentonites and Smectite-Rich Clay Materials.” *SKB Technical Report*, 112.
White, G. Norman, and L. W. Zelazny. 1988. “Analysis and Implications of the Edge Structure of Dioctahedral Phyllosilicates.” *Clays and Clay Minerals* 36 (2): 141–46. https://doi.org/10.1346/CCMN.1988.0360207.

7. Appendix

Figure contents

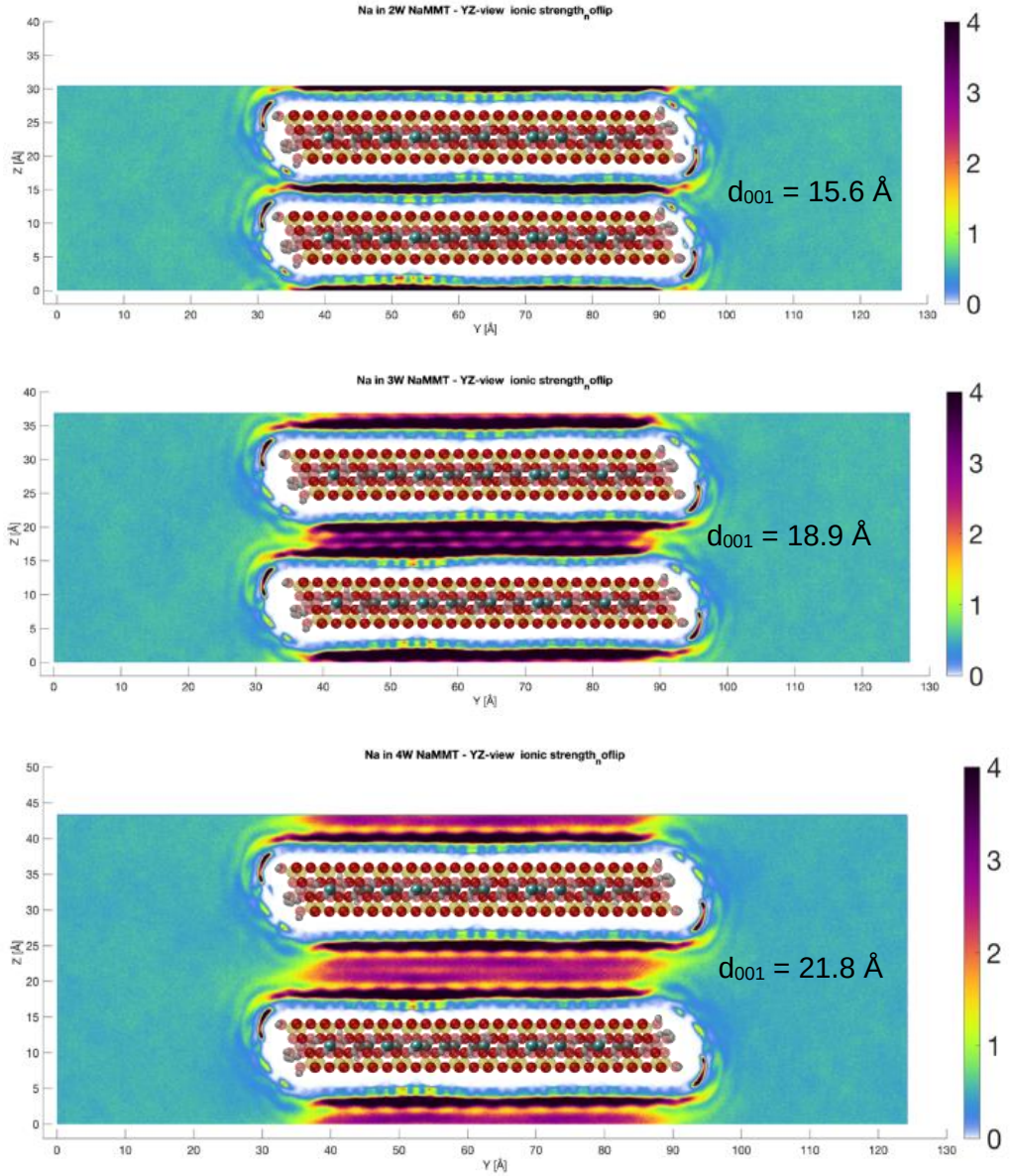

Figure S1. Collage of clay layers and 2D concentration maps of Na^+ ions in the 2W (top), 3W (middle) and 4W (bottom) system, shown along the X direction in the YZ-plane. Color bar on the right indicate concentrations in [moles/L].

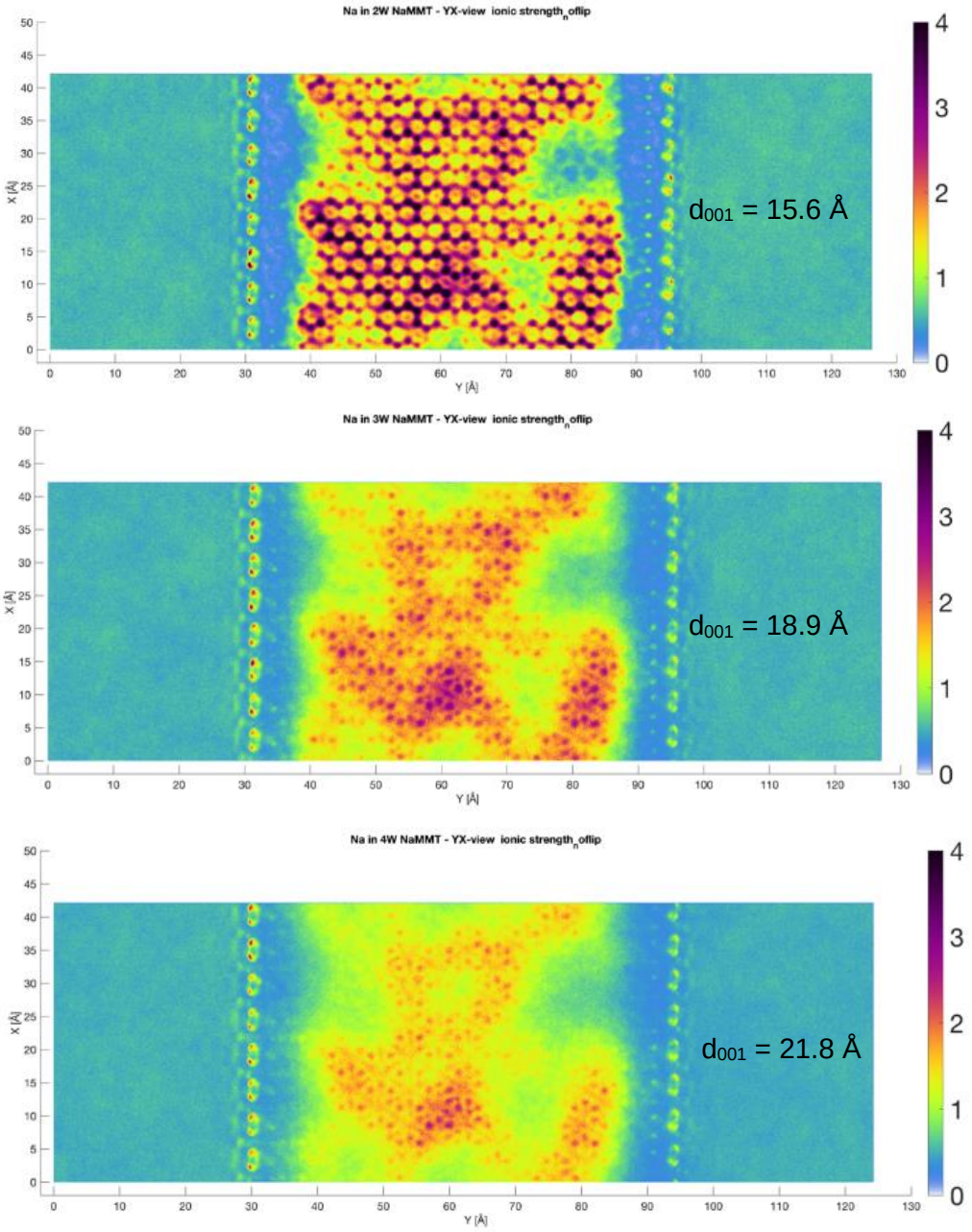

Figure S2. 2D concentration maps of Na^+ ions in the 2W (top), 3W (middle) and 4W (bottom) system, shown along the Z direction in the YX-plane within a single interlayer. Color bar on the right indicate concentrations in [moles/L].

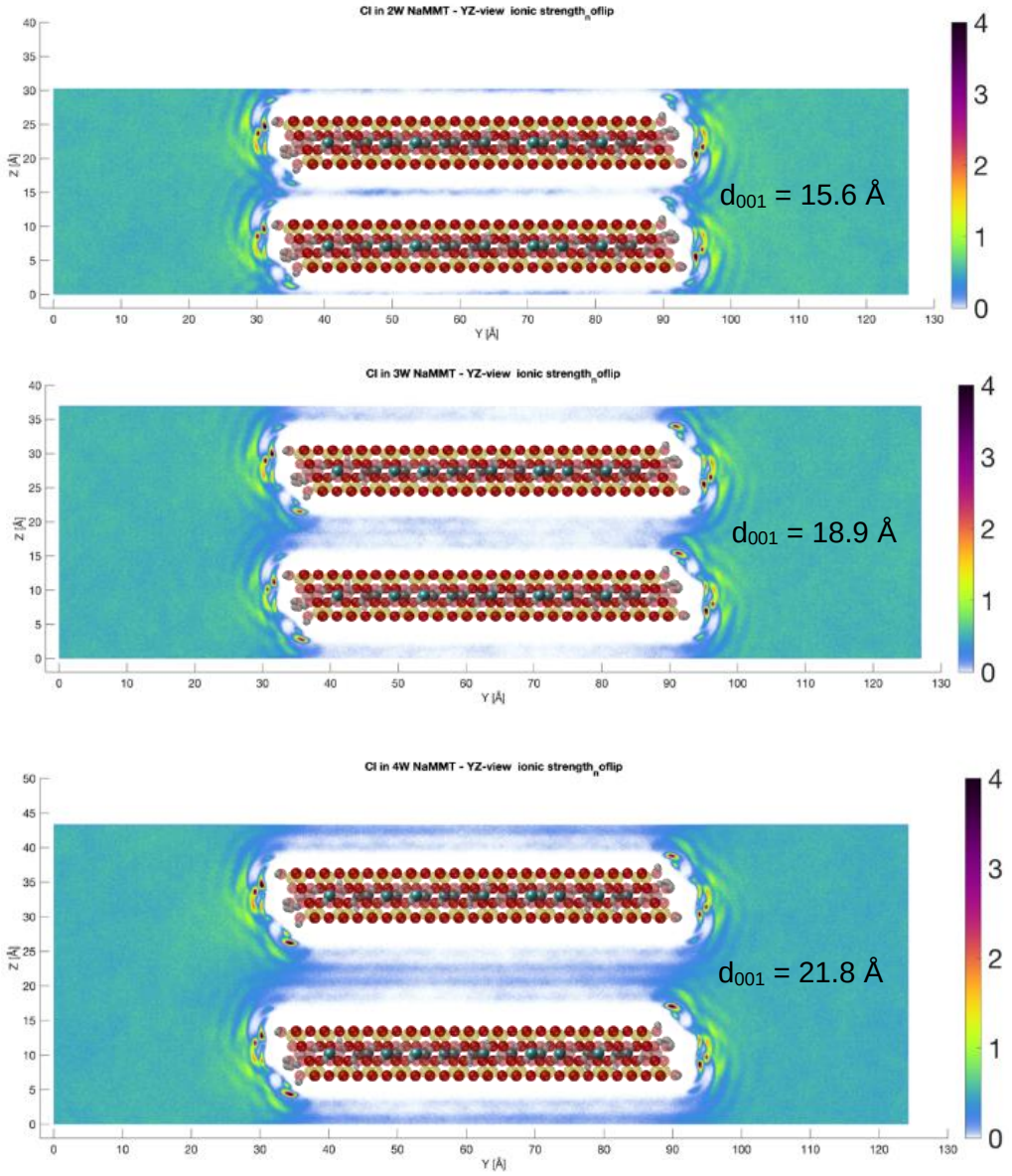

Figure S3. Collage of clay layers and 2D concentration maps of Cl^- ions in the 2W (top), 3W (middle) and 4W (bottom) system, shown along the X direction in the YZ-plane. Color bar on the right indicate concentrations in [moles/L].

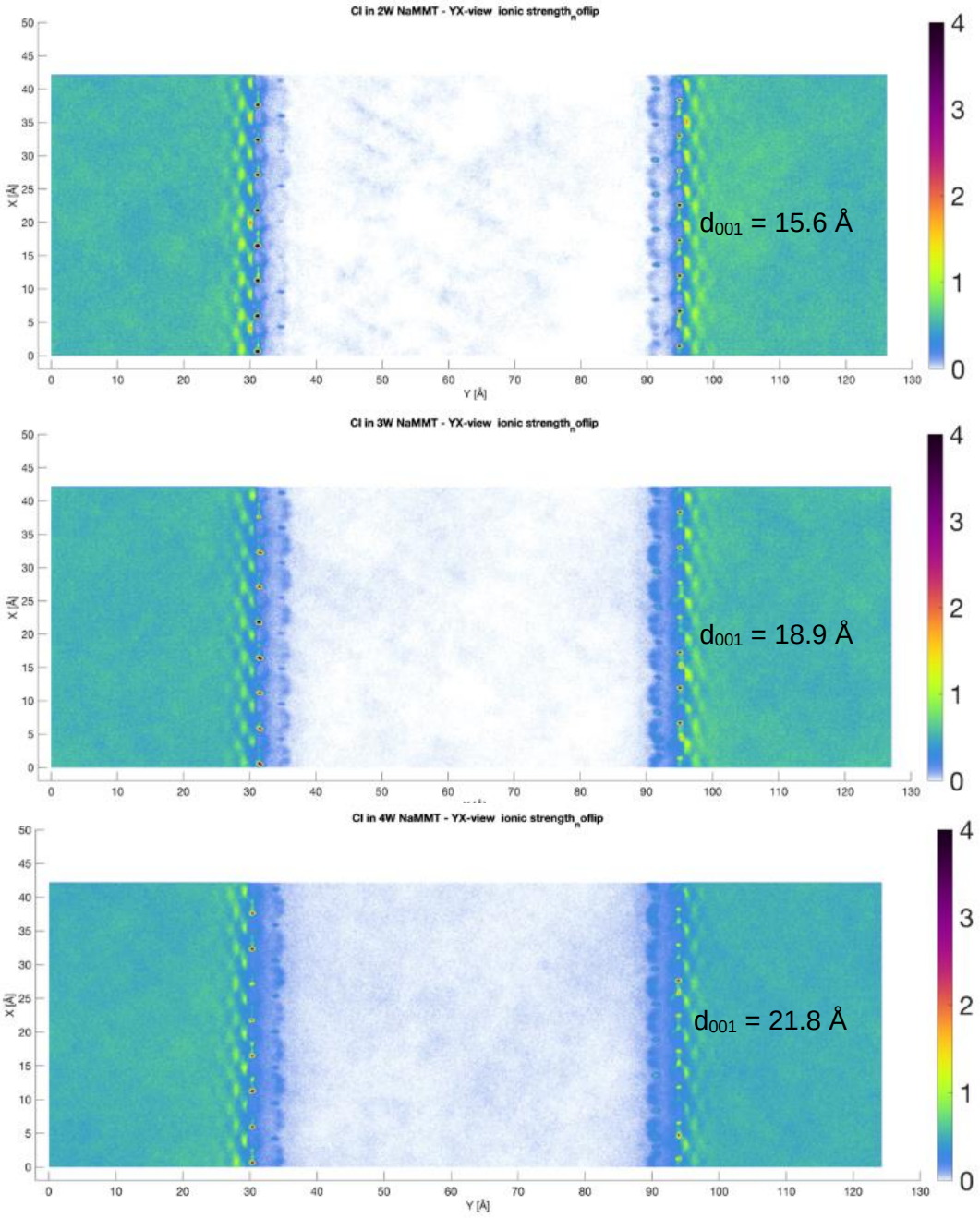

Figure S4. 2D concentration maps of Cl^- ions in the 2W (top), 3W (middle) and 4W (bottom) system, shown along the Z direction in the YX-plane within a single interlayer. Color bar on the right indicate concentrations in [moles/L].

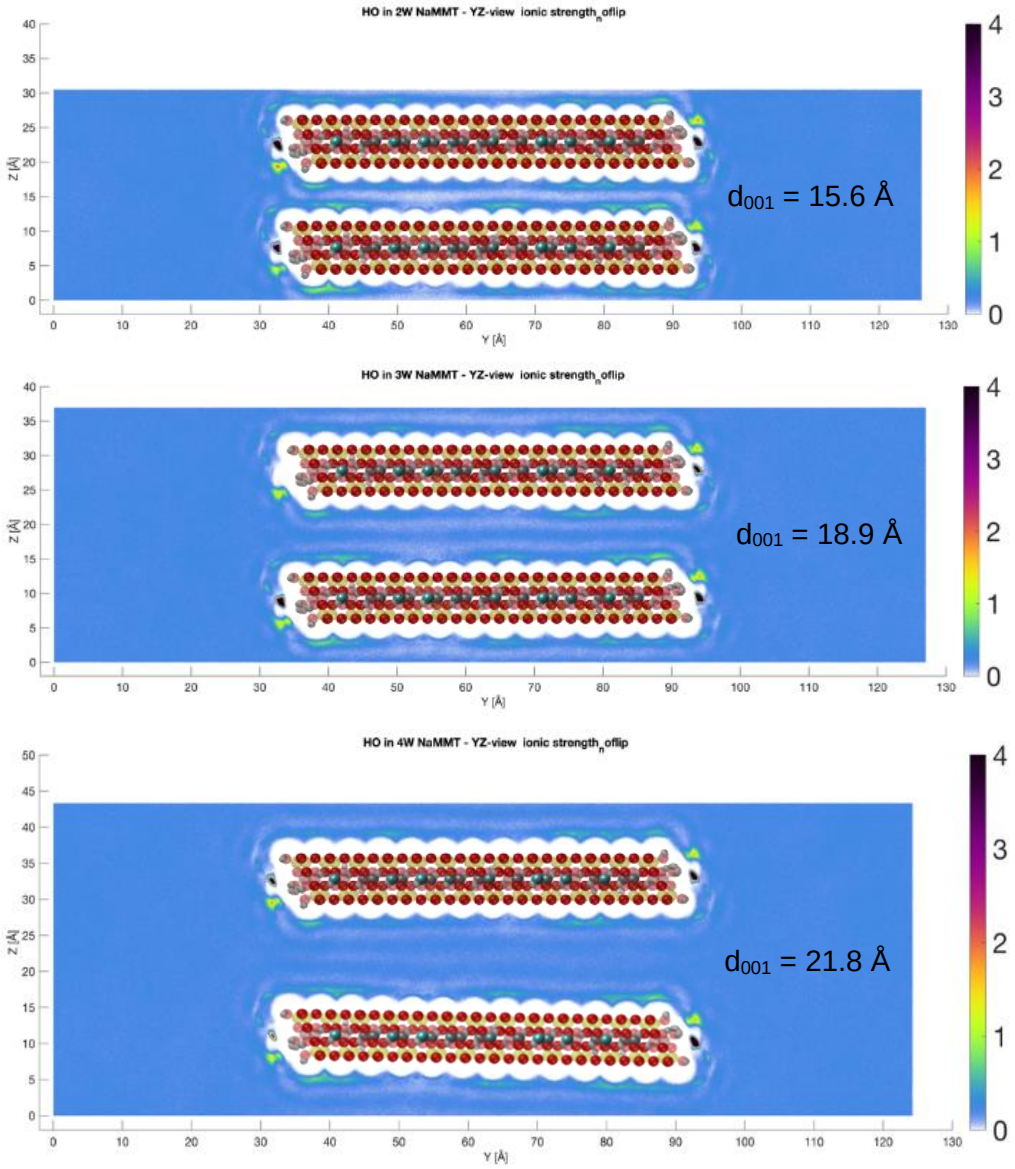

Figure S5. Collage of clay layers and 2D concentration maps of HO• radicals in the 2W (top), 3W (middle) and 4W (bottom) system, shown along the X direction in the YZ-plane. Color bar on the right indicate concentrations in [moles/L].

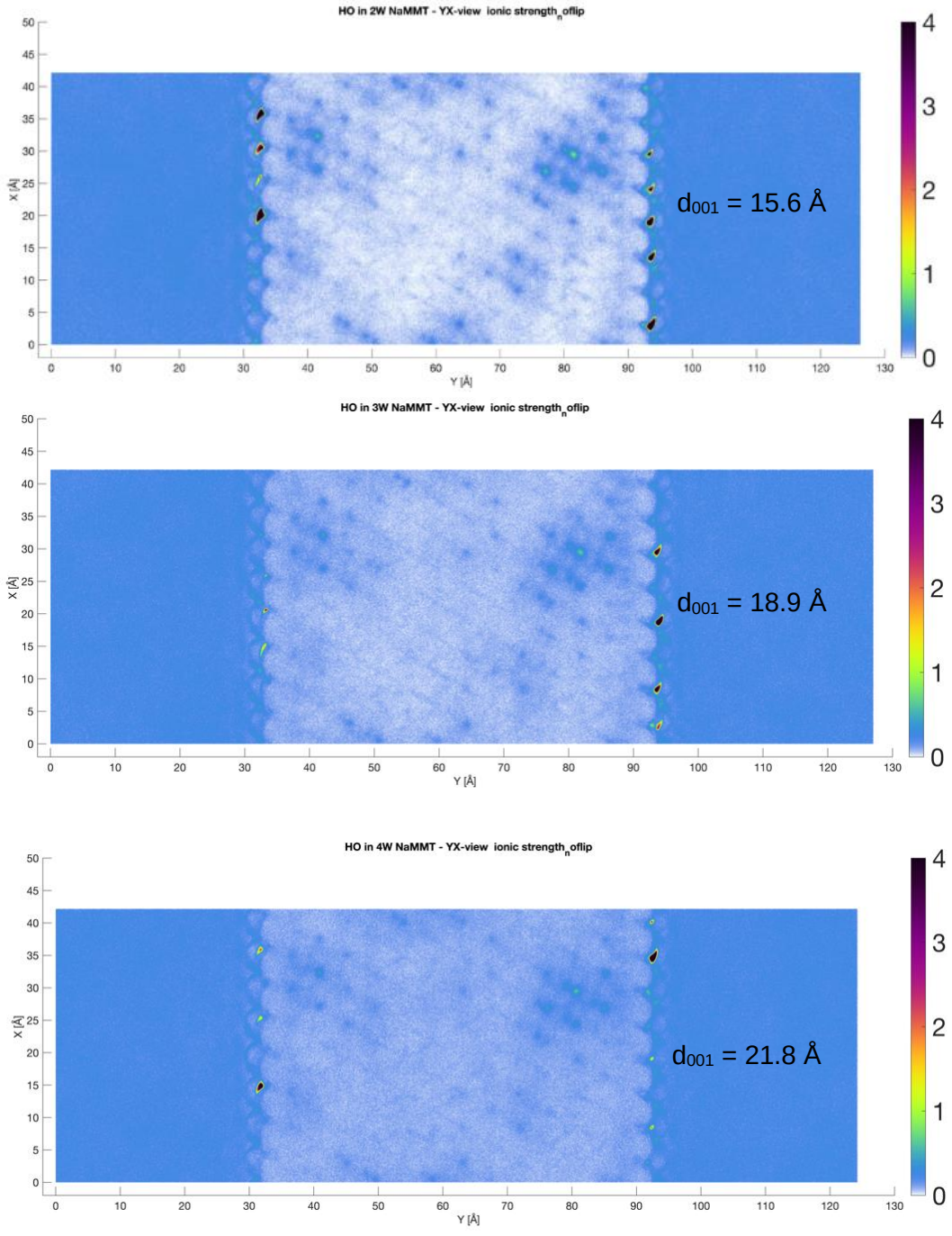

Figure S6. 2D concentration maps of HO• radicals in the 2W (top), 3W (middle) and 4W (bottom) system, shown along the Z direction in the YX-plane within a single interlayer. Color bar on the right indicate concentrations in [moles/L].

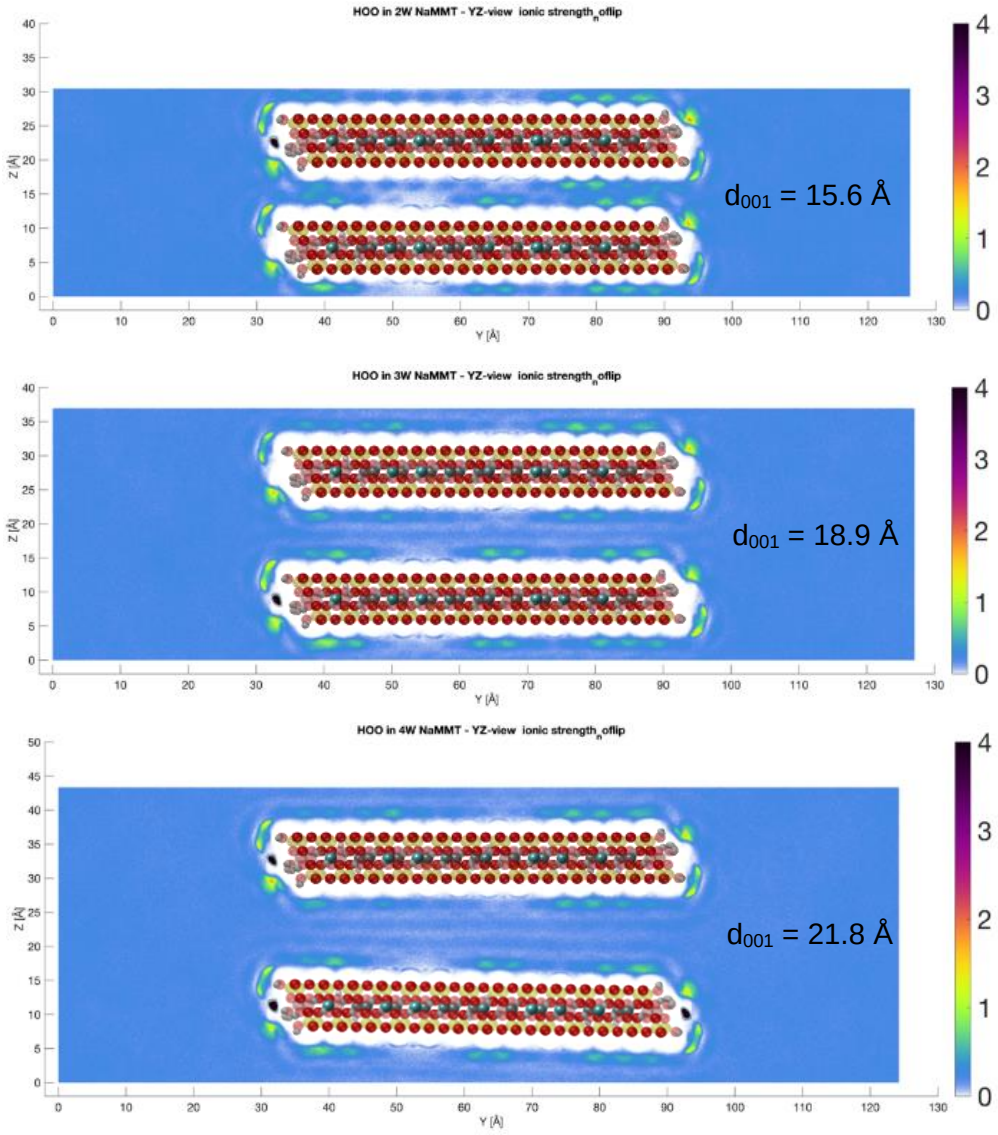

Figure S7. Collage of clay layers and 2D concentration maps of HOO• radicals in the 2W (top), 3W (middle) and 4W (bottom) system, shown along the X direction in the YZ-plane. Color bar on the right indicate concentrations in [moles/L].

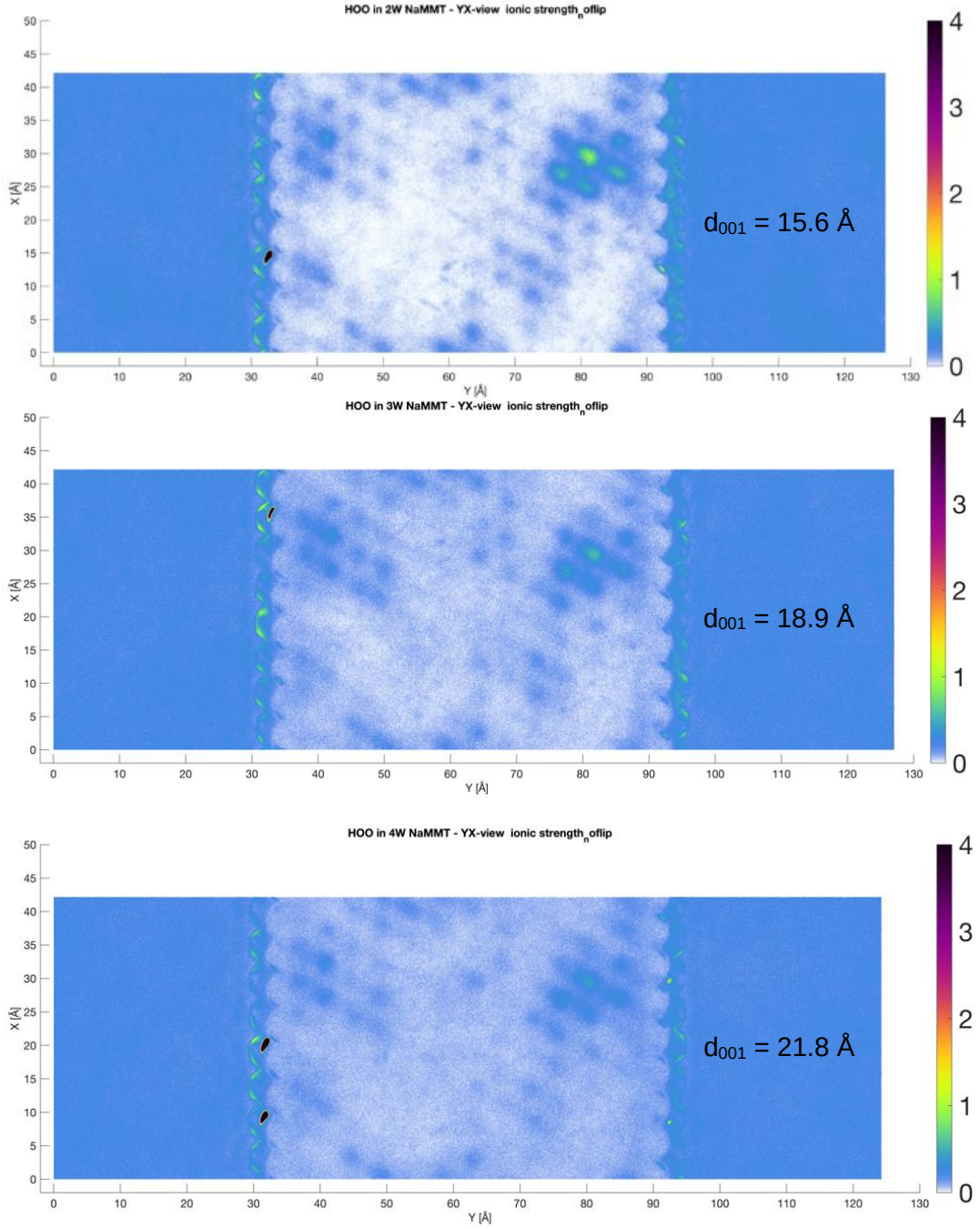

Figure S8. 2D concentration maps of HOO• radicals in the 2W (top), 3W (middle) and 4W (bottom) system, shown along the Z direction in the YX-plane within a single interlayer. Color bar on the right indicate concentrations in [moles/L].

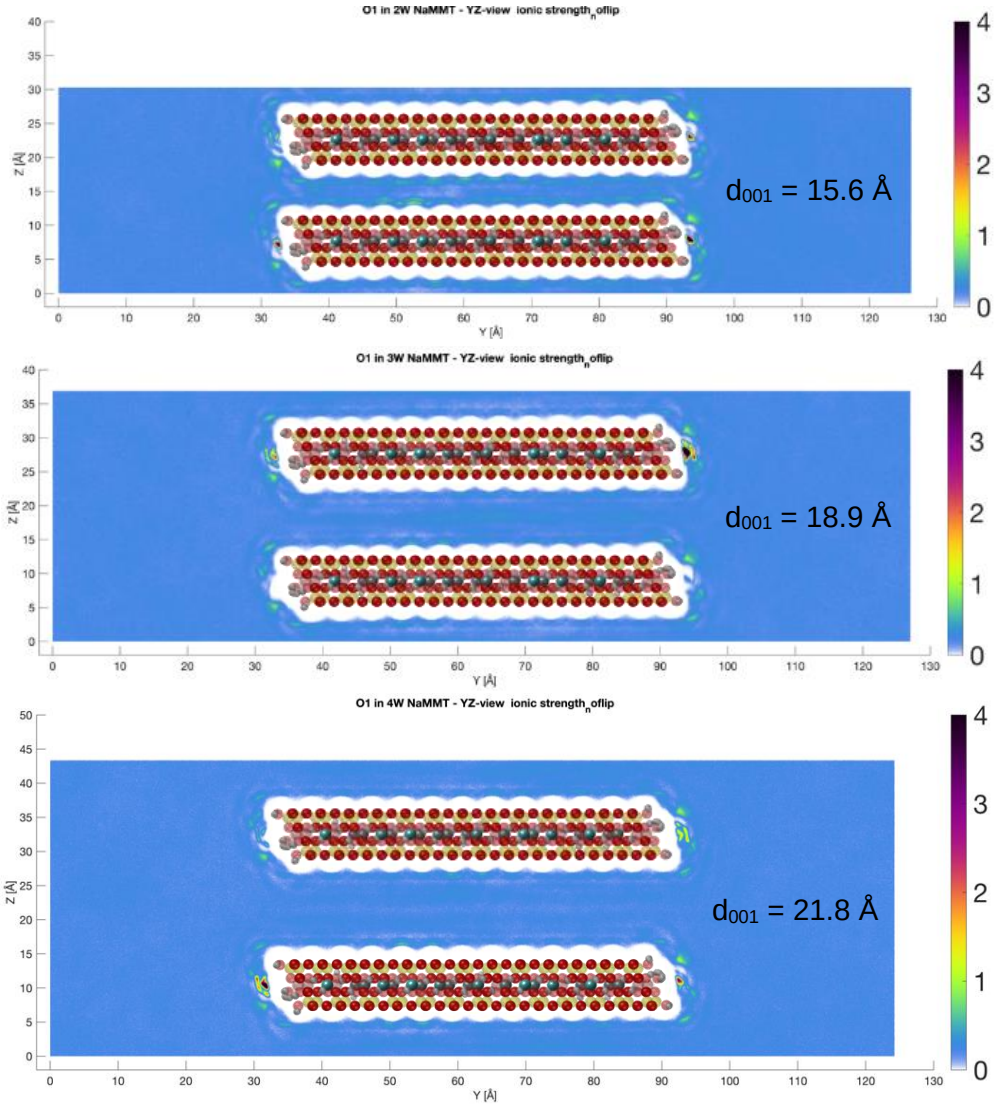

Figure S9. Collage of clay layers and 2D concentration maps of the oxygen atoms in H_2O_2, in the 2W (top), 3W (middle) and 4W (bottom) system, shown along the X direction in the YZ-plane. Color bar on the right indicate concentrations in [moles/L].

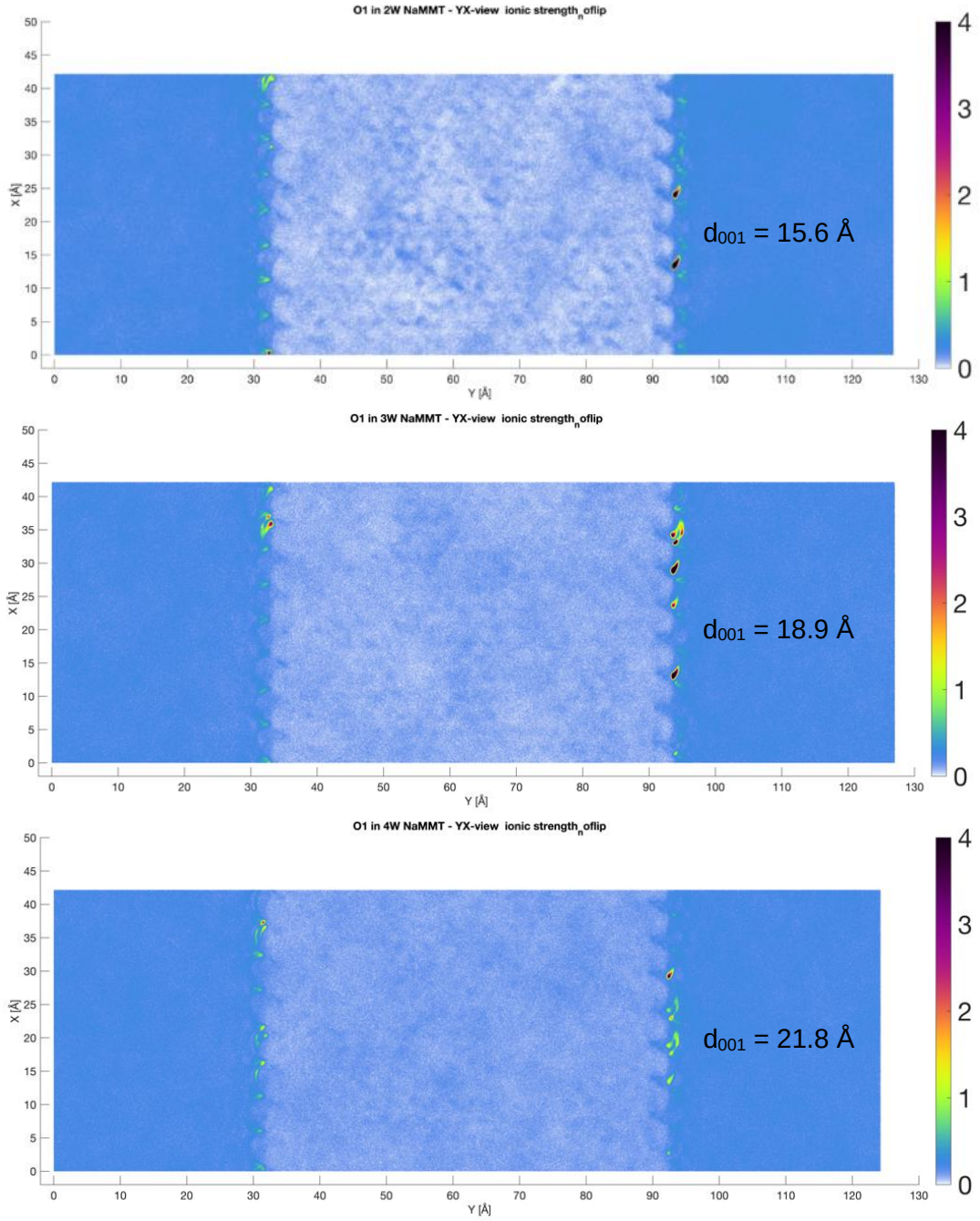

Figure S10. 2D concentration maps of the oxygen atoms in H_2O_2, in the 2W (top), 3W (middle) and 4W (bottom) system, shown along the Z direction in the YX-plane within a single interlayer. Color bar on the right indicate concentrations in [moles/L].

The Swedish Radiation Safety Authority (SSM) works proactively and preventively with nuclear safety, radiation protection, nuclear security, and nuclear non-proliferation to protect people and the environment from the harmful effects of radiation, now and in the future.

You can download our publications from www.stralsakerhetsmyndigheten.se/en/publications. If you need alternative formats such as easy-to-read, Braille or Daisy, contact us by email at registrator@ssm.se.

Strålsäkerhetsmyndigheten
SE-171 16 Stockholm
+46 (0) 8-799 40 00
www.stralsakerhetsmyndigheten.se
registrator@ssm.se

E-print AB, 2023